

Tectonic patterns on Vesta and Ceres revealed by polygonal impact craters

Hiu Ching Jupiter Cheng ^{a,b,*}, Christian Klimczak ^b

^a Department of Geological Sciences, University of Alabama, Tuscaloosa, AL 35401, USA

^b Center for Planetary Tectonics at UGA, Department of Geology, University of Georgia, Athens, GA 30602, USA

ARTICLE INFO

Keywords:

Vesta
Ceres
Impact cratering
Planetary tectonics

ABSTRACT

Polygonal impact craters (PICs), impact craters with straight rims that form polygonal shapes in plan-view, form where pre-existing structures exist in the impact target rock. The straight rim segments of PICs and their preferred orientations are known to reveal hidden tectonic patterns that otherwise are invisible in spacecraft data. Vesta and Ceres are heavily cratered bodies that also experienced tectonics. We systematically mapped crater rims on Vesta and Ceres with crater diameters ≥ 10 and 20 km, respectively. We identified and extracted straight rim segments that maintain consistent orientations for at least 5 km to assess their segment lengths and orientations. The majority of mapped craters on Vesta and all craters on Ceres have at least one straight rim segment and thus are considered PICs. Analyses of straight rim segment orientations reveal multiple fracture sets that form complex but systematic regional and global patterns on both bodies. In particular, we detected an E–W trending fracture pattern in Vesta’s north-polar region. Ceres predominantly shows NE–SW oriented fractures in the northern hemisphere and NW–SE oriented fractures in the southern hemisphere that are most pronounced at the poles. None of these patterns correlate with the orientations of large-scale troughs on Vesta and pit chains on Ceres or with large impact basins on Vesta, indicating that their origins are not directly linked. Their differing tectonic patterns indicate that different planetary processes controlled the formation of fractures responsible for the straight rim segments of the PICs. We compare our identified fracture patterns with predicted tectonic patterns caused by changes in spin rate, volume change, and true polar wander. However, predictions of tectonic patterns in the existing literature are not specific to, and thus not applicable to Vesta and Ceres, requiring more detailed modeling efforts and rock-mechanical reassessments to investigate the underlying processes that produced the fracture sets.

1. Introduction

1.1. Tectonics of polygonal impact craters

Polygonal impact craters (PICs) abound on all cratered planetary bodies in the solar system, including Earth (e.g., Meteor Crater in Arizona; Shoemaker, 1960), the Moon (e.g., Shoemaker, 1962; Baldwin, 1963; Öhman et al., 2010; Weber et al., 2022), Mercury (e.g., Wood et al., 1977; Weihs et al., 2015; Yazici et al., 2024), Venus (e.g., Aittola et al., 2007; Aittola et al., 2010), Mars (e.g., Binder and McCarthy Jr., 1972; Öhman et al., 2006, 2010; Watters et al., 2011), icy moons (e.g., Beddingfield et al., 2016; Neidhart et al., 2017; Beddingfield and Cartwright, 2020), and asteroids (Prockter et al., 2002; Neidhart et al., 2017; Weber et al., 2022). PICs provide information about the crustal structure and properties of the target planetary body. Numerous studies have characterized and catalogued PICs (e.g., Weihs et al., 2015; Neidhart

et al., 2017; Zeilhofer and Barlow, 2021a), studied their global distribution (e.g., Weihs et al., 2015; Zeilhofer and Barlow, 2021a), investigated their cratering mechanics (e.g., Öhman et al., 2008), and examined their relationship with regional tectonics (e.g., Aittola et al., 2010; Beddingfield et al., 2016; Beddingfield and Cartwright, 2020; Zeilhofer and Barlow, 2021a).

PICs are defined as having at least one straight rim segment in plan view, often with two segments intersecting at an angle (e.g., Tabares-Rodenas et al., 2013; Beddingfield et al., 2016; Zeilhofer and Barlow, 2021a; Robbins and Riggs, 2023). The presence of pre-existing structures in the target rock influences the formation of PICs, as these structures are reactivated or utilized during the excavation or modification stages of the cratering process if they are suitably located or oriented (e.g., Schultz, 1976; Öhman et al., 2006; Kumar and Kring, 2008). These structures include various types of faults (e.g., Öhman et al., 2008; Dasgupta et al., 2019; Beddingfield et al., 2024; Baby et al.,

* Corresponding author at: Department of Geological Sciences, University of Alabama, Tuscaloosa, AL 35401, USA.

E-mail address: hhansen2@ua.edu (H.C.J. Cheng).

2024), joints (e.g., Öhman et al., 2005, 2006), and structural weaknesses paralleling fold axes (e.g., Poelchau et al., 2009), which will all be referred to as fractures in this work.

Multiple studies have proposed models of pre-existing fractures affecting the formation of PICs, distinguishing between simple and complex craters. Based on the observations of the square-shaped Meteor Crater in Arizona, excavation of simple craters was proposed to be more efficient along the pre-existing fractures, forming straight crater rims diagonal to those fractures (Eppler et al., 1983; Poelchau et al., 2009). In contrast, Kumar and Kring (2008) reported the rims of Meteor Crater are parallel to three prominent sets of pre-impact fractures, instead of their diagonals. They proposed that materials were preferentially overturned or slumped along the fractures during excavation for simple craters. For complex craters, Eppler et al. (1983) proposed that slumping takes place preferably along pre-existing fractures during the modification stage, causing straight rims to form parallel to fractures. Moreover, Öhman (2009) suggested that thrusting along pre-existing fractures late in the excavation stage causes straight crater rims to be parallel to the fracture orientations for both simple craters (e.g., Meteor Crater) and small to mid-sized complex craters (e.g., in the Argyre region on Mars). Straight crater rims are also observed to align parallel to pre-existing fractures at Tswaing Crater in South Africa and Endurance Crater on Mars (e.g., Öhman, 2009; Watters et al., 2011), as well as on other planetary bodies (Beddingfield et al., 2016; 2024; Beddingfield and Cartwright, 2020).

For PICs on other planetary bodies, pre-existing fractures may be hidden beneath the regolith layer or exist on scales lower than the resolution of spacecraft imagery. Straight rim segments reveal these fractures, allowing the study of surface or subsurface fracture patterns that would otherwise remain hidden in the geological record. Although the type of structures and the subsurface geometry (e.g., the dip angle of the fault plane) of pre-existing fractures cannot be determined from individual straight rim segments, their orientations (i.e., the strike) can be interpreted as a regional or global tectonic pattern considering the different PIC formation models (e.g., Eppler et al., 1983; Kumar and Kring, 2008; Poelchau et al., 2009; Öhman, 2009). These patterns can be compared to that of other planetary bodies and to predicted tectonic patterns formed by various planetary processes, such as global contraction (Byrne et al., 2014) or expansion (Melosh and McKinnon, 1988), large-scale impact cratering (Asphaug et al., 1996), true polar wander (Matsuyama and Nimmo, 2011), and change in spin rate (Matsuyama and Nimmo, 2008; Beuthe, 2010).

1.2. PICs on Ceres

NASA's Dawn mission (Russell and Raymond, 2011) revealed a variety of tectonic landforms on Ceres (e.g., Buczkowski et al., 2016), including faults, ridges, scarps, fractures, troughs/grooves, pit crater chains, lineaments, and PICs. Since the first descriptions of PICs on Ceres (e.g., Hiesinger et al., 2016), several studies examined such structures. Otto et al. (2016) reported 258 PICs on Ceres with diameters between 5 km and 280 km, the majority of which are 10 to 50 km in diameter with a mean of 21 km. Neidhart et al. (2017) studied 90 craters on Ceres and found 63 (70 %) of them to be polygonal with diameters between 8 and 280 km, most of which have diameters of 10 to 40 km. The number of straight rims was found to range between two and seven.

Zeinhofer and Barlow (2021a) reported that among the 44,594 craters in their near-global crater database of Ceres, 1466 are PICs (~3.3 %). They characterized these PICs according to their relationships with structures outside or inside the crater. Most of the characterized PICs were not found to be related to any visible structures. Hexagonal crater shapes are the most common with an average interior angle between straight rim segments of ~122°. Linear features, i.e., Junina and Samhain Catena were found to be accompanied by PICs (Zeinhofer and Barlow, 2021a). The Junina Catena were interpreted as secondary crater chains whereas the Samhain Catena were interpreted to be structural, forming pit crater chains (Buczkowski et al., 2016; Scully

et al., 2017). Moreover, PICs were identified throughout different stages of crater degradation, indicating that pre-existing fractures have influenced the formation of PICs on Ceres since its earliest preserved geologic record. The northern latitudes have a higher polygonal crater density than the southern latitudes (Otto et al., 2016; Zeinhofer and Barlow, 2021a), which may indicate crustal heterogeneity across Ceres (e.g., Ammannito et al., 2016; Konopliv et al., 2018) or resurfacing of the southern hemisphere by younger and larger impact basin (i.e., Urvara and Yalode basins) that pre-date a proposed true polar wander event at the early history of Ceres (Tricarico, 2018).

1.3. PICs on Vesta

Although documented by a handful of studies, PICs on Vesta have received less attention than those on Ceres, and their underlying tectonics have not yet been studied. PICs were first described by Ruesch et al. (2014), and Neidhart et al. (2017). The latter study identified 90 craters with a diameter range of 3.1 to 53.2 km, where 50 (56 %) of them were found to be polygonal. Most of these PICs were reported to have diameters between 10 and 30 km. The number of straight crater rims was found to range from two to seven.

Vesta has two sets of large-scale troughs with the younger Divalia Fossae encircling two-thirds of the equator and the older Saturnalia Fossae present in the northern hemisphere. Both structures were proposed to be formed by the impact that formed the Rheasilvia and Veneneia basins near the south pole (e.g., Jaumann et al., 2012; Buczkowski et al., 2012). Weber et al. (2022) conducted a regional study of the two regions near these trough systems. Of the 48 craters surveyed, only 8 (~17 %) were identified as PICs. The most common number of straight rim segments found was four, with an average angle of 132°– between them. These particular PICs are not located near any visible tectonic structures, and thus they were hypothesized to have been influenced by buried fractures.

1.4. Objective of this study

Previous studies of PICs on Vesta and Ceres visually selected craters and their straight rim segments. They investigated mainly the crater sizes, spatial distributions, number of straight rim segments, angles between straight rim segments, and length of the straight rim segments (e.g., Otto et al., 2016; Neidhart et al., 2017; Zeinhofer and Barlow, 2021a). The orientations of straight rim segments have yet to be analyzed, and therefore any hidden tectonic patterns have not yet been explored. While impact craters in general have previously been mapped globally (e.g., Williams et al., 2018; Yingst et al., 2014), PICs and their straight rim segments have not been specifically mapped and studied globally. Furthermore, tectonic patterns in the lithosphere, if and where they occur, are largely hidden under the widespread and thick regolith cover on Vesta and Ceres (e.g., Prettyman et al., 2017; Parekh et al., 2021). Using PICs to uncover hidden tectonic patterns, especially where mapped and assessed using a well-defined mapping protocol to detect straight rim segments quantitatively, enables us to learn about the tectonics of Vesta and Ceres and to compare them to one another.

This work aims to identify and analyze the orientations of straight rim segments on Vesta and Ceres to explore if they reveal previously hidden local, regional, or even global tectonic patterns. To do that, we quantify the number, length, and orientation of straight rim segments. The orientations of all straight crater rim segments are then visually and statistically analyzed to investigate whether they display preferred orientations. Preferred orientations can be compared to orientations of nearby tectonic landforms on Vesta and Ceres to examine if they could have utilized the same pre-existing fractures. We adopted the parallel relationship between straight rim segments and pre-existing fractures in this study, as it is supported by models for simple and complex craters (e.g., Öhman, 2009), as well as observations on other planetary bodies (e.g., Öhman, 2009; Beddingfield et al., 2016; 2024). Building upon this,

we also compare regional and global tectonic patterns revealed by PICs to previous predictions of tectonic patterns for a series of planetary processes that could have influenced the tectonics on the two largest bodies in the asteroid belt.

2. Methodology

2.1. Datasets and mapping

This study used the Dawn Framing Camera (FC; Sierks et al., 2011) image mosaics and digital terrain models (DTMs) acquired from the NASA Planetary Data System. For Vesta, the High Altitude Mapping Orbit (HAMO) global mosaic has a resolution of 60 m/px (Roatsch et al., 2013), and the DTM has a resolution of 70 m/px (Preusker et al., 2016a). For Ceres, the HAMO global mosaic has a resolution of 140 m/px (Roatsch et al., 2016), and the DTM has a resolution of 137 m/px (Preusker et al., 2016b). We primarily used HAMO data due to the better coverage and illumination of Vesta's north pole, which exhibits PICs, and the data resolution is sufficient for the selected sizes of craters in this study.

We acquired the impact craters in this study from the global crater catalogs of Vesta (Liu et al., 2018) and Ceres (Hiesinger et al., 2016), with these catalogs containing 11,605 craters with diameters ≥ 0.7 km on Vesta and 531 craters with diameters ≥ 20 km on Ceres. All impact structures with diameters ≥ 10 km on Vesta and ≥ 20 km on Ceres were mapped, because these size ranges capture most of the previously reported PICs on Vesta and Ceres and are available in the catalogs (Hiesinger et al., 2016; Liu et al., 2018). Because the orientations of rims of large impact basins would dominate the length-weighted analysis (described in the next section), we exclude the > 400 km diameter Veneneia and Rheasilvia basins on Vesta but present their basin-bounding scarps as large-scale tectonic structures on the global maps for comparison. Our mapping includes partially superposed craters, as some straight rim segments may remain preserved. As cratering is a stochastic process, we do not anticipate that mapping partially preserved craters would bias the tectonic patterns. On the contrary, excluding partially preserved craters would bias the results toward the most recently emplaced craters. Each crater was recorded with a unique identification number and its center coordinates to produce the catalogs for Vesta and Ceres as shapefiles (available in Appendix C supplementary data; Cheng, 2024).

Following the study by Yazici et al. (2024), we define a crater rim as the most elevated region surrounding the topographic depression caused by the impact, often showing a raised edge. All mapping was carried out using ESRI ArcGIS software and followed a defined data collection protocol for consistency in data collection over the entire surfaces of Vesta and Ceres. Since the recognition and mapping of crater shapes are highly subjective and depend on the mapping scale, basemaps were reprojected to the cataloged centers for each crater using a stereographic projection at a fixed mapping scale of 1:200,000. This mapping scale allows for clear observation of crater rims and their geometries even for the smallest considered craters in the chosen dataset.

To detect straight segments of crater rims and thus identify PICs, we devised a method closely following that previously used and rigorously tested for craters on Mercury (Yazici et al., 2024). We illustrated the outcome of the method with examples of craters displaying a planform polygonal shape on Vesta (Fig. 1) and Ceres (Fig. 2). All rims were mapped as polylines with regularly spaced vertices of 1 km for both Vesta and Ceres (Figs. 1b, 2b), using the streaming function of the ArcMap Editor to ensure consistent data sampling. We applied the line simplification function on the mapped polyline (Fig. 1c). This function simplifies polylines by connecting the endpoints of a line with a straight line and removing redundant vertices, which are closer to the trend line than the set tolerance. The applied tolerances for Vesta and Ceres were selected to be ~ 0.5 km and ~ 1 km, respectively. The lower applied tolerance on Vesta better captures straight rim segments from less

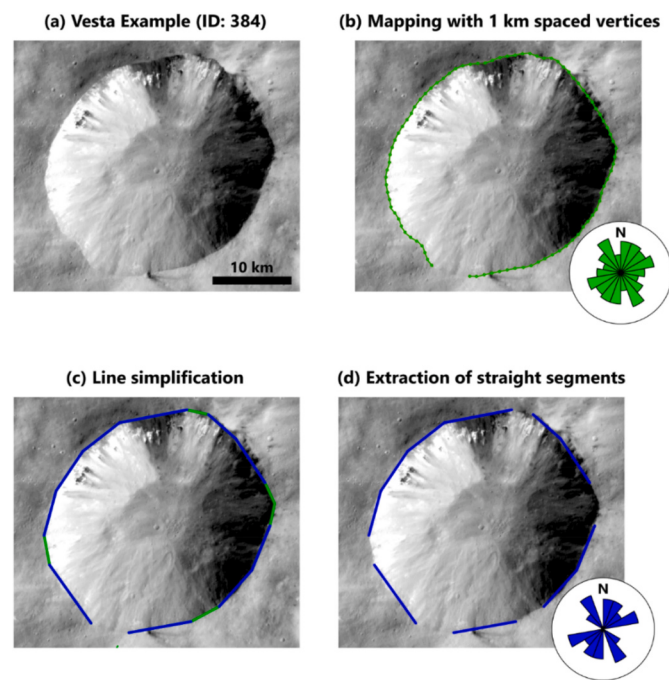


Fig. 1. An example of the plan view of impact crater geometry, showing how the mapping and straight segments extraction methods work on ArcMap. (a) A crater displaying a planform shape on Vesta (centered at 7.394°S and 37.486°E). (b) The rim is mapped as a polyline (green lines) with 1 km spaced vertices (green dots). (c) Straight rim segments are simplified and longer sections were identified (blue lines with a length ≥ 5 km). (d) By deleting short segments, straight rim segments are extracted and rose diagrams can be plotted to visualize their orientations. The rose diagram in (d) accentuates the preferred orientations of straight rim segments as compared to (b). (For interpretation of the references to colour in this figure legend, the reader is referred to the web version of this article.)

obvious PICs (see Fig. 1), whereas a higher value applied to craters on Ceres performs better for more obvious PICs (see Fig. 2). A tolerance ranging from half to one vertex spacing (i.e., 0.5 and 1 km) returns a simplified crater shape that is in close agreement with the originally mapped polyline. The simplified polylines were split at the remaining vertices. Following this simplification process, a curved crater rim segment should retain more vertices than a straight one, such that after splitting, the straight segments should be longer, and the curved segments should be shorter (Fig. 1c). After testing various segment lengths and tolerances, we found that segments with a length ≥ 5 km return geologically meaningful results of straight rim segments on either body with the selected crater sizes on Vesta and Ceres (Fig. 1d). A longer segment length would result in straight segments in smaller craters being omitted, while a shorter cut-off could lead to curved segments in larger craters being misidentified as straight segments.

This method was tested for a complex situation showing multiple, superposed craters on Ceres (Fig. 2a). All crater rims are mapped using streaming (Fig. 2b), followed by extracting the straight rim segments (Fig. 2c) as outlined above. We extract the orientations of straight rim segments by computing their azimuths and plotting them in rose diagrams, which are circular histogram plots that display directional data. A detailed explanation of the visualization of the orientation data is given in section 2.2. The orientation distribution of all mapped rims in our sample areas (Figs. 1b, 2b), shows a wide spread of orientations resulting from curved rim segments and degradation of the crater rim. After simplification, the orientation distributions contain only straight rim segments and thus are more representative of any underlying tectonic patterns (Fig. 2c). We classified craters with at least one straight segment extracted as PICs, and all remaining craters as circular craters.

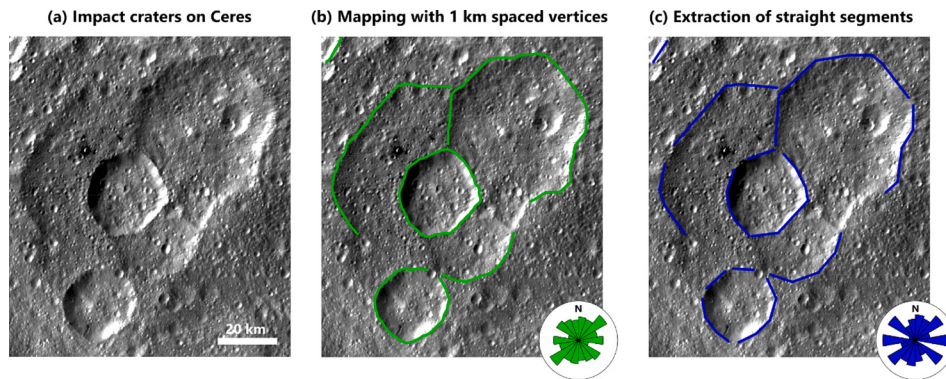


Fig. 2. Planform shapes of typical impact craters on Ceres showing stages of data collection. (a) View of typical PICs on Ceres in Dawn Ceres FC image mosaic centered at 23.657°N and 64.473°W. (b) The crater rims are mapped as polylines using streaming shown as green lines. (c) After performing line simplification on the mapped polylines, straight crater rim segments are extracted (blue lines) as those longer than 5 km. Length-weighted rose diagrams of (b) and (c) are plotted in green and blue, respectively, for comparison. (For interpretation of the references to colour in this figure legend, the reader is referred to the web version of this article.)

We visually verified each simplified crater rim if it matched the planform shape of the crater in the photogeology. Craters with simplified polylines that mismatched the shape were recorded in the dataset but excluded from further analysis. We tested our mapping workflow with four different mappers and demonstrated the robustness and efficacy of the manual mapping procedure in [Yazici et al. \(2024\)](#).

2.2. Visual and statistical analyses

Length-weighted rose diagrams were produced to visualize the orientations of all mapped crater rims as well as for straight rim segments only across the surface of Vesta and Ceres. We split all polylines at their vertices and calculated the true lengths and true orientations (i.e., the strike) of all resulting segments using the Tools for Graphics and Shapes plug-in ([Jenness, 2011](#)) for ArcMap 10.8 to avoid errors caused by projection distortions that are unaccounted for in the ArcMap toolbox. We plot rose diagrams for all mapped crater rims (always shown in green) and also for extracted straight crater rims (always shown in blue). To generate length-weighted rose diagrams for all crater rims, all our mapped crater rim segment orientations were plotted, as they were all 1 km long. For length weighting the extracted straight rim segments, the calculated length of these segments was rounded down to the nearest whole number in km and plotted as the counts of the orientations.

The choice of bin size for the rose diagrams is based on the total length of the segments considered for each diagram. We calculated bin degree width (b) as a relationship of range (R) and sample size (N) where $b = R / (2 N^{1/3})$ ([Freedman and Diaconis, 1981](#); [Sanderson and Peacock, 2020](#)). We used the range of $R = 360^\circ$, but for evaluating orientations of fracture planes where the dip is unknown, only a scale of 0° to 180° is needed as strike values between 180° and 360° can be mirrored by those between 0° to 180° . The sample size is reported as the total length of all segments in kilometers. We rounded the calculated values of bin width to the nearest whole, even number, allowing us to split 180° evenly into bins. By doing so, rose diagrams in areas with a greater sample size will show more details in the overall orientations whereas those with a smaller sample size will show a more general distribution without being unnecessarily complex for interpretation.

The crater segments and rose diagrams for Vesta and Ceres were plotted on global tectonic maps for visualization and comparison. These bodies were binned into six 30° latitudinal bands and twelve 30° longitudinal strips to analyze the rose diagrams globally. We further assessed regional patterns on Vesta and Ceres by generating rose diagrams for 18 regions that have comparable surface areas to one another. Specifically, the regions consist of one polar, three mid-latitude, and five equatorial regions per hemisphere. Additionally, these 18 regions were plotted on Vesta using concentric and radial boundaries centered on the

Rheasilvia basin to test whether any global tectonic patterns corresponding to the impact could be detected.

We applied the Kuiper test for uniformity ([Kuiper, 1960](#)) to determine if the orientations of the mapped crater rims and straight rim segments have preferred orientation(s) using the open-access software environment for statistical computing and graphics, R ([R Core Team, 2022](#)). The null hypothesis is that the orientation distribution for crater rims in an area is uniform, assuming that planform crater shapes are completely circular and that the superposition of impact crater happens randomly. If this Kuiper test returns p -values that are less than an alpha level of 0.05, there are preferred orientations of crater rims with 95 % confidence. We chose the Kuiper test of uniformity because it is based on plotting the cumulative frequency without binning of data. This allows preferred orientations to be identified and the departure from a uniform orientation distribution to be recognized without a binning bias. In particular, many visually assessed plots may have been interpreted as showing preferred orientations, whereas the null hypothesis of uniformity is accepted based on the data, especially when the sample size is small. Rose diagrams with uniform distributions and preferred orientations were labeled in the global maps to aid interpretations.

A different statistical approach for identifying PICs was developed and applied for Dione ([Beddingfield et al., 2016](#)) and Miranda [Beddingfield and Cartwright, 2020](#)). However, this method applies only to craters with a complete rim preserved, which is rarely the case on Vesta and Ceres. This approach would skew the data toward the best preserved and generally youngest craters. Since the straight rim segments from all PICs, including those that are partly preserved, are important to identify hidden fracture sets over the entire preserved geological history, we did not adopt the previous methodology.

3. Mapping results and comparison to tectonic structures

3.1. Vesta

The global crater catalog of Vesta ([Liu et al., 2018](#)) contains 412 craters with diameters ≥ 10 km. We mapped the rims of 408 impact craters ([Fig. 3a](#)) and omitted four craters from the mapping because they were too degraded to map any rim segments. Eight craters, all with diameters less than 15 km, were excluded from analyses owing to a mismatch of simplified polylines with the crater shapes or false returns of straight segments. Out of the remaining 400 analyzed impact craters, 301 (~75.4 %) craters are classified as PICs with at least one straight rim segment extracted ([Fig. 3a](#); supplementary data).

In the latitudinal binning ([Fig. 3a](#), rose diagrams on the left), all crater rims have non-uniform orientations north of 30° S ([Fig. 3a](#), green rose diagrams), and uniform orientations southward of 30° S ([Fig. 3a](#),

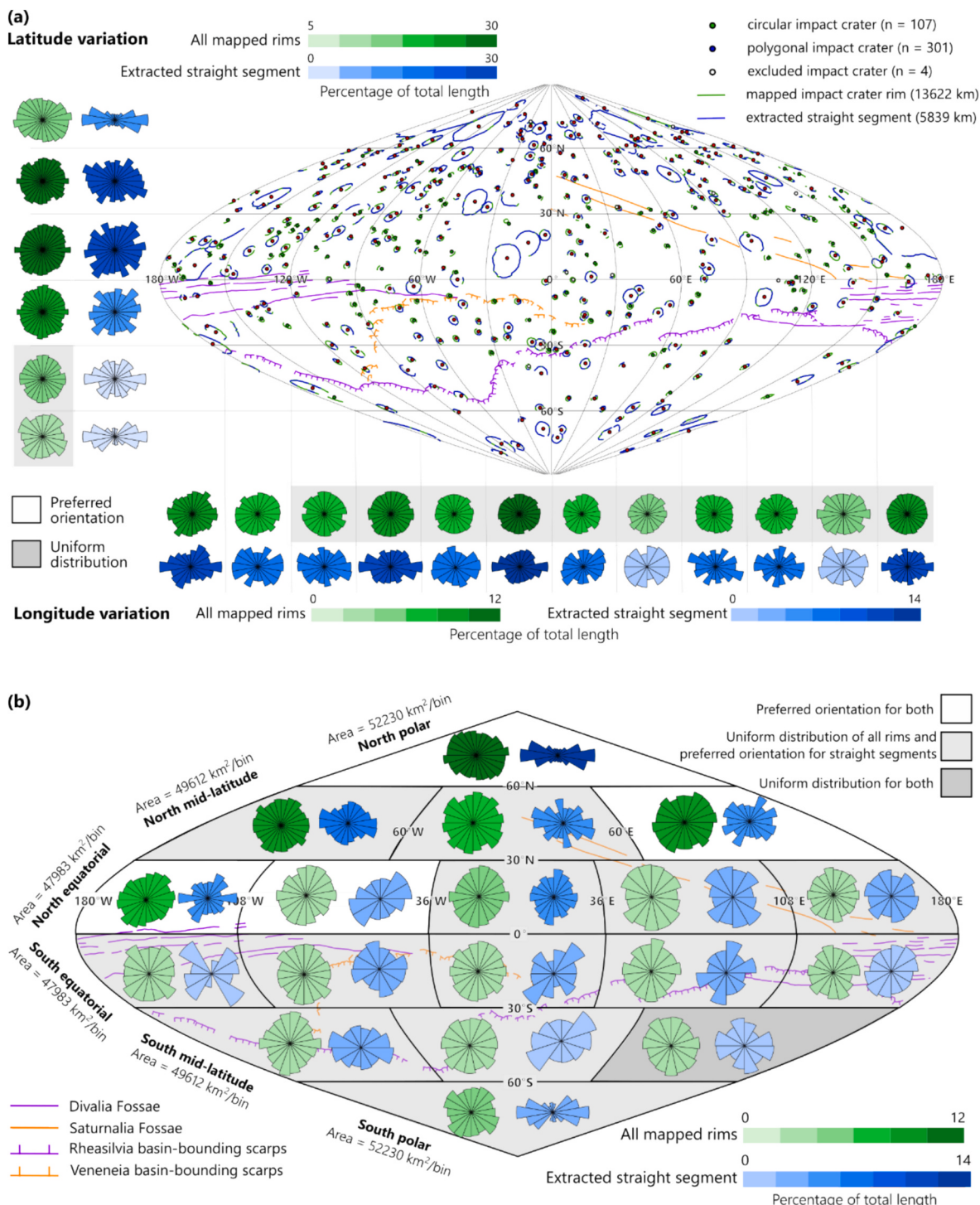


Fig. 3. Global map of Vesta in sinusoidal projection showing the mapping of crater rims and their orientations in different geographic bins. For comparison to crater data, the basin-bounding scarps of the Rheasilia and Veneneia basins, Divalia Fossae, and Saturnalia Fossae are plotted. (a) All crater rims and straight rim segments and their orientations are displayed in rose diagrams shown in green and blue, respectively. The center coordinates for each crater, including circular, polygonal, or those that were excluded, are plotted with a point symbol. Length-weighted rose diagrams are plotted in 30° latitudinal bands and longitudinal strips, with colour intensity indicating the percentage they contribute toward the overall dataset. Rose diagrams statistically determined to show a uniform distribution are shaded in gray. (b) Orientations of all crater rims (green) and straight rim segments (blue) are shown as rose diagrams for each of the 18 equal-area regions. Rose diagrams for all crater rims statistically determined to show a uniform distribution are shaded in light gray, those with uniform distribution for all crater rims and straight rim segments are shaded in dark gray. All rose diagrams have the north direction pointing toward the top of the figure. (For interpretation of the references to colour in this figure legend, the reader is referred to the web version of this article.)

gray shading; Appendix A Table A1). All latitudinal regions show preferred orientations for straight rim segments (Fig. 3a, blue rose diagrams; Appendix A Table A2). All crater rims and extracted straight rim segments both exhibit a strongly E–W preferred orientation in the north polar region, indicating the presence of a fracture set with such orientations influencing the shapes of impact craters. Multiple preferred orientations are present between 60°N and 30°S for all crater rims and only straight rim segments (Fig. 3a). This indicates that the northern mid-latitudes and equatorial regions are fractured by several sets of moderately preferred orientations, including N–S, NE–SW, E–W, and SE–NW. While the orientations of all crater rims between 30°S to 90°S are uniformly distributed, the extracted straight rim segments show a strongly E–W preferred orientation (Fig. 3a). This indicates the presence of an E–W oriented fracture pattern near the south pole, mirroring the pattern of the north pole. In the south, this pattern does not substantially influence the overall shape of craters. Moderately preferred NE–SW and SE–NW orientations are also present in the southern mid-latitudes (Fig. 3a), indicating this region is fractured by at least three major fracture sets.

As for the longitudinal binning, most longitudes show a uniform orientation distribution of all crater rims, except for regions between 120°W to 180°W (Fig. 3a; Appendix A Table A3). However, most longitudes show E–W preferred orientations and one or more additional preferred orientations for the straight rim segments (Fig. 3a; Appendix A Table A4). Overall, no clear systematic change in pattern is noticeable across the longitudinal regions, indicating that the observed orientation distributions are primarily influenced by the latitudinal patterns of fracture systems.

We divided Vesta into 18 equal-area regions to investigate any regional preferred orientations of crater rims. Four regions have preferred orientations for all crater rims and straight rim segments and those are all in the northern hemisphere (Fig. 3b, not shaded). The north polar region shows a strongly E–W preferred orientation, the same finding as in the latitudinal analysis (Fig. 3b). Out of all regions, 14 regions show uniform orientation distributions of all crater rims (Fig. 3b; Appendix A Table A5), but 13 of those do show a preferred orientation distribution of the straight rim segments (Fig. 3b light gray shaded; Appendix A Table A6). This indicates that multiple fracture sets are present throughout Vesta, but they do not have a significant effect on the overall crater shapes in these regions. The southern mid-latitudinal region between 60°E and 180°E is the only region that shows uniform orientations for all crater rims and straight rim segments (Fig. 3b, dark gray shaded). Visually, the rose diagram of straight rim segments appears to have preferred orientations of E–W and NW–SE, but statistically they are considered not significant likely due to the small sample size.

We compared the crater data with the basin-bounding scarps of the Rheasilvia and Veneneia basins mapped in Cheng and Klimczak (2022a), as well as the large-scale troughs of Divalia Fossae and Saturnalia Fossae mapped in Cheng and Klimczak (2022b). Divalia and Saturnalia Fossae overlap only with regions that have a uniform orientation distribution of all crater rims (Fig. 3b), indicating that the large-scale troughs do not affect the overall shapes of the impact craters. Regions where the Divalia Fossae are present also lack dominant E–W preferred orientations for the straight rim segments, indicating PICs and the Divalia Fossae did not share the same pre-existing fracture sets. The straight rim segments in the north mid-latitudinal region between 60°W to 60°E have a preferred orientation that matches with the orientation of the Saturnalia Fossae (i.e., NW–SE). However, the orientation distributions of the straight segments in other regions overlapping with the Saturnalia Fossae (i.e., 36°E to 180°E at the north equatorial region) do not share the same NW–SE orientations, indicating that PICs did not share the same pre-existing fracture sets with the Saturnalia Fossae and that other hidden structures influenced the crater geometries. Moreover, the preferred orientations of the straight rim segments do not match with the basin-bounding scarps of Rheasilvia and Veneneia, which should be predominantly ~E–W at the south equatorial and mid-latitude regions (Fig. 3b),

indicating these basin-bounding scarps did not influence the formation of PICs.

To investigate if PICs utilized fracture systems as part of a damage zone introduced to Vesta's lithosphere by the Rheasilvia impact, we divided Vesta into equal-area regions with basin-concentric and basin-radial boundaries and re-calculated length-weighted rose diagrams for each of these regions (Fig. 4; Appendix A Tables A7 and A8). To aid the descriptions, we labeled the regions from RH1 at the center of the basin to RH18 at the antipode of the basin, and the colour-coding of diagrams for all crater rims and straight rim segments as well as shading for tests of uniformity remains as in Fig. 3. Generally, it is common to find structures that formed radially or concentrically within or around impact craters and basins, such as on Earth (e.g., Osinski and Spray, 2005; Kumar and Kring, 2008), Mars (e.g., Carr et al., 1977; Öhman et al., 2005), the Moon (e.g., Krishna and Kumar, 2016), and icy moons (e.g., Moore et al., 2004). Some bins around the Rheasilvia basin show basin-radial components (RH9 and RH16) or basin-concentric components (RH3 and RH4). However, no consistent and systematic basin-related pattern is noticeable in the other regions. Therefore, it remains unclear how far the observed basin-radial and concentric orientations truly utilized fractures from impact damage caused by the Rheasilvia impact. Thus, PICs do not show a widespread, noticeable relationship to the Rheasilvia basin, not allowing us to detect the presence and extent of the impact damage zone. One possible reason for the lack of a widespread relationship is that the Rheasilvia impact, with an estimated age as recent as ~1.0 billion years (Marchi et al., 2012; Schenk et al., 2012), occurred relatively late in Vesta's geological history. By this time, the lithosphere was likely already extensively fractured by previous impacts including that forming the Veneneia basin (Cheng and Klimczak, 2022a), obscuring a clear pattern from the Rheasilvia impact. Additionally, some PICs may also predate the Rheasilvia impact such that their straight rim segments would not reflect a Rheasilvia impact damage zone.

3.2. Ceres

Of the 531 craters cataloged on Ceres (Hiesinger et al., 2016), 525 impact craters were analyzed. Six craters were omitted because they were too degraded to identify any rim segments. No mismatches of simplified polylines with the crater shapes or false returns of straight segments were detected. All of the analyzed craters have at least one straight rim segment and are classified as PICs (Fig. 5a; supplementary data), with the vast majority of them forming clear hexagonal planform shapes (see examples in Fig. 2), confirming previous findings (e.g., Otto et al., 2016; Zeilhofer and Barlow, 2021a).

As with Vesta, we analyzed crater rim orientations on Ceres by latitude and longitude. All latitudinal bands show non-uniform orientation distributions for all crater rims and straight rim segments (Fig. 5a; Appendix B Tables B1 and B2), indicating the presence of one or more preferred orientations of fractures. The orientation distributions for all crater rims and straight rim segments, i.e., the shapes of the rose diagrams (Fig. 5a) are similar to one another for each of the geographical regions because most crater rims were identified as straight rim segments. This shows that Ceres's lithosphere is fractured by several major joint sets, which govern the planform shape of all craters. The northern hemisphere shows preferred NE–SW to E–W orientations at the polar and mid-latitudinal regions and NW–SE to N–S orientation at the equator. The southern hemisphere shows preferred NW–SE to E–W orientations, which are most pronounced at the south pole (Fig. 5a).

Along the longitudinal strips, seven out of 12 regions have non-uniform orientation distributions of all crater rims (Fig. 5a; Appendix B Table B3). All regions but one show preferred orientations of straight rim segments (Fig. 5a; Appendix B Table B4), and all of the rose diagrams indicate one or more preferred orientations, confirming the presence of several major fracture sets across Ceres. However, no distinctive systematic patterns or variations of orientations stand out

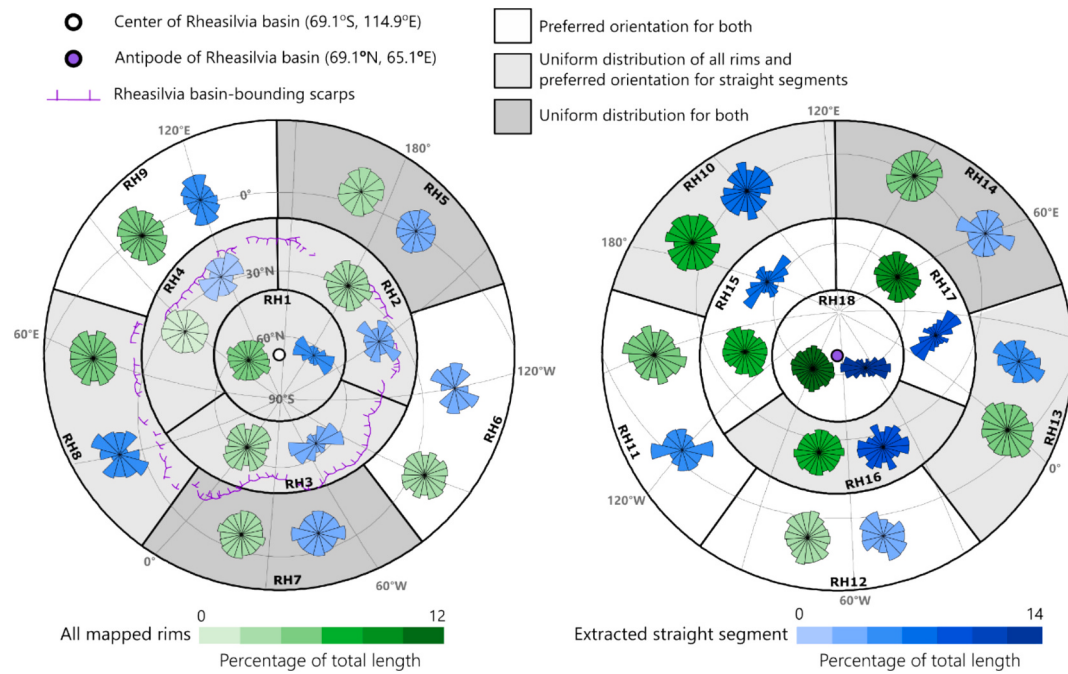


Fig. 4. Global map of Vesta shown as two stereographic projections centered on the Rheasilvia basin on the left and the Rheasilvia basin antipode on the right with 18 basin-radial/concentric regions. The colour-coding and shading of the length-weighted rose diagrams follow Fig. 3. All rose diagrams are rotated to align with the cardinal directions on the map. (For interpretation of the references to colour in this figure legend, the reader is referred to the web version of this article.)

along the longitudes.

We divided the globe of Ceres into 18 equal-area regions to investigate any regional patterns of preferred orientations of crater rims (Fig. 5b; Appendix B Tables B5 and B6). All regions but one show preferred orientations for all crater rims, but all regions show preferred orientations of straight rim segments. The orientation distributions for all crater rims and extracted straight rim segments are similar, confirming that the impact crater shapes are dominated by straight rim segments in all parts of Ceres. A trend similar to that seen in the latitudinal variations of preferred orientations (Fig. 5a) is confirmed throughout the regions (Fig. 5b). All polar and mid-latitudinal regions in the northern hemisphere have a preferred NE-SW orientation component, and some also have other preferred orientations, and preferred NW-SE and N-S orientations at the equator. Most regions in the southern hemisphere show a pronounced preferred NW-SE orientation, except for the southern equatorial regions between 36°E to 180°E. These findings indicate that the latitudinal variation of preferred orientations is a global, widespread pattern on Ceres.

Pit crater chains were previously compared with PICs on Ceres. Zeilhofer and Barlow (2021a) reported that Junina and Samhain Catena have the most number of related PICs based on their spatial relationship which was defined to be the maximum distance of 10 crater radii with relation to the pit chain system. To test if their formation involves the same pre-existing fracture sets, we compare these two previously mapped catenae to the orientations of straight crater rims extracted in this study (Fig. 5b). Preferred orientations of straight rim segments show NW-SE trends in the south equatorial regions between 180°W to 36°W, which are partly consistent with the mapped orientations of the Samhain Catenae. This NW-SE tectonic pattern occurs not only near these catenae but also across the entire equatorial region and throughout the southern hemisphere (Fig. 5b). However, while a few straight rim segments in the region around the Junina Catena match in orientations, the most pronounced preferred orientations of straight crater rim segments are nearly perpendicular to those of the Junina Catena (i.e., north equatorial region between 180°W to 36°W). This indicates that Junina Catena form independently of the pre-existing structures influencing PICs, agreeing with the interpretation that the

catenae are secondary crater chains (Buczkowski et al., 2016; Scully et al., 2017). Our findings thus do not show a well-defined relationship between the catenae and PICs. The fracture systems revealed by PICs are not only localized around the structures but are present throughout a larger region affecting most of the northern hemisphere (Fig. 5). Hence, the high number of PICs reported near Junina and Samhain Catena (Zeilhofer and Barlow, 2021a) likely reflects the large area covered by these two pit crater chains but does not prove any relationship between the formation of PICs and the pit chains.

4. Latitudinal variations in tectonic patterns on Vesta and Ceres

The results of this work indicate that latitudinal variations in tectonic patterns are revealed by PICs on Vesta and Ceres, though these patterns differ between the two bodies. On Vesta, a prominent east-west trending fracture system is evident in the north polar regions that is potentially mirrored at the south pole (Fig. 3), suggesting that specific tectonic processes produced these preferred orientations and thus influenced the planform shapes of craters. In contrast, the equatorial and mid-latitudinal regions exhibit less systematic patterns, showing no clear relationship with large-scale troughs (Fig. 3b) or impact basins (Figs. 3b and 4). This indicates that Vesta contains fractures of all orientations, consistent with a highly fractured asteroid subjected to billions of years of impact bombardment. These fractures have not healed or annealed, aligning with previous findings by Cheng and Klimczak (2022a), and the straight crater rim segments are a reflection of these fractures. However, due to the random orientation of the fractures, they do not significantly affect the overall shape of the craters in these regions, resulting in a mostly random distribution of all crater rim orientations (Fig. 3b).

Strongly preferred fracture orientations vary latitudinally on Ceres (Fig. 5a). The northern polar and mid-latitudinal regions from about 30°N to 90°N have a dominant fracture system showing preferred orientations of NE-SW, whereas the tectonic patterns become NW-SE trending in the southern hemisphere, especially toward the south pole (Fig. 5). These findings suggest that tectonic processes produced preferred orientations, influencing the overall planform of crater shapes. Unlike Vesta where the preferred orientations of the straight rim

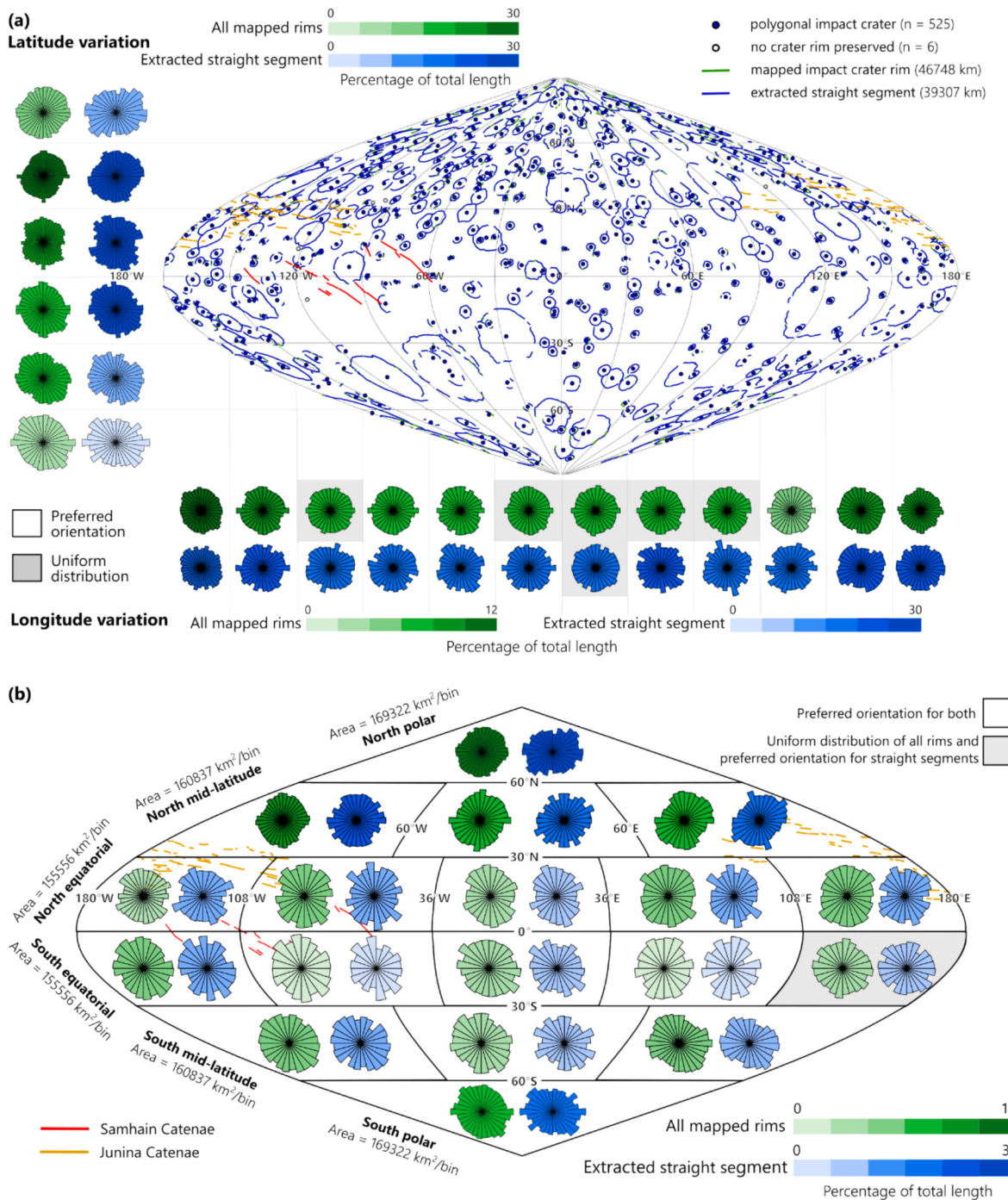


Fig. 5. Global map of Ceres in sinusoidal projection showing outlines of crater rims and their orientations in different geographic bins. For comparison to crater data, the pit crater chains of the Samhain and Junina Catena are plotted. (a) Map of all crater rims and straight rim segments showing orientations in rose diagrams. The center coordinates for each crater, including circular, polygonal, or those that were excluded, are plotted with a point symbol. Length-weighted rose diagrams are plotted in 30° latitudinal bands and longitudinal strips, with colour intensity indicating the percentage they contribute toward the overall dataset, where green rose diagrams represent all mapped rims and blue rose diagrams represent extracted straight rim segments. Rose diagrams statistically determined to show a uniform distribution are shaded in gray. (b) Orientations of all crater rims (green) and straight rim segments (blue) are shown as rose diagrams for each of the 18 equal-area regions. Rose diagrams for all crater rims statistically determined to show a uniform distribution are shaded in light gray, those with uniform distribution for all crater rims and straight rim segments are displayed shaded in dark gray. All rose diagrams have the north direction pointing toward the top of the figure. (For interpretation of the references to colour in this figure legend, the reader is referred to the web version of this article.)

segments do not significantly affect the overall crater shapes, these tectonic patterns are not only observed for the extracted straight rim segments but also dictate the overall shape of craters across Ceres. Hence, straight rim segments form more efficiently on Ceres, possibly because pre-existing fractures, particularly multiple intersecting sets,

are more pervasive across the surface.

The tectonic patterns revealed by PICs on Ceres do not show a clear relationship with the Junina and Samhain Catena, indicating that their formation is unlikely to be related to the same processes causing the fracture sets that shaped the crater rims. This finding aligns with

Buczkowski et al. (2016) and Scully et al. (2017), who proposed that the Junina Catena are secondary crater chains. These chains are non-radial to any specific source, likely due to Ceres' rapid rotation and low gravity, which may be associated with the Urvara and Yalode impacts. The Samhain Catena were proposed to form from extension caused by upwelling convection or diapirism at Hanami Planum (Scully et al., 2017). Zeilnhofer and Barlow (2021a) suggest that maximum tensile stresses are perpendicular to the structural orientation of the Samhain Catena, which may influence the shape of the smaller PICs, reaffirming that PICs formed in a location adjacent to the pit crater chains. However, the NW–SE fracture systems revealed by the PICs are not confined to the area around Samhain Catena but instead extend over a larger region, possibly encompassing most of the southern hemisphere (Fig. 5), indicating a global or hemispheric tectonic process rather than one confined to the regions affected by the pit chains.

Processes hypothesized to have caused global tectonic patterns on minor bodies mainly include stresses from rotational bulging and large impacts (Thomas and Prockter, 2010). However large impacts, such as the impact forming the Rheasilvia basin, lack any relationship with the tectonic patterns on Vesta (Fig. 4), and Ceres lacks very large impact basins altogether (Marchi et al., 2016). Stresses from rotational bulging could potentially cause global tectonic patterns, as Vesta and Ceres have fast rotation periods of ~5 and 9 h, respectively. Although the faster rotation rate of Vesta as compared to Ceres would likely induce different stress magnitudes on the planetary surface, the modes of stress and their global distributions when forming an equatorial bulge may be comparable. Therefore, if fast rotation and equatorial bulging were to be the only cause of the tectonic patterns on Vesta and Ceres, any latitudinal pattern revealed by straight crater rim segments would be expected to be similar between the two bodies. However, the observed latitudinal variations of tectonic patterns do not compare well to one another. Therefore, the fracture patterns on the two bodies are unlikely to be solely driven by tectonics from fast rotation.

Moreover, Vesta and Ceres have very different compositions. Vesta has a dry, basaltic crust (e.g., Zellner et al., 1997; McCord and Scully, 2015), whereas Ceres has an icy crust mixed with rocky materials (e.g., Castillo-Rogez et al., 2018). Crater morphology and the simple-to-complex crater transition of craters on Ceres support a relatively weak target compared to the fractured crystalline rock of Vesta (e.g., Buczkowski et al., 2016; Hiesinger et al., 2016). However, the difference in crustal mechanical properties is unlikely to influence the PIC distribution and their tectonic patterns. In fact, Ceres is heavily cratered with craters on the scale studied here not showing to be majorly affected by viscous relaxation (e.g., Zeilnhofer and Barlow, 2021a; Schenk et al., 2021). Therefore, Ceres has PICs of different ages distributed and preserved globally, similar to the crater distribution observed on rocky bodies like Vesta. Although there is no consensus on the mechanics of PIC formation in icy versus rocky targets, straight rim segments are widely observed to align with pre-existing fractures on rocky bodies (e.g., Öhman, 2009; Watters et al., 2011; Beddingfield et al., 2024) and icy bodies (e.g., Beddingfield et al., 2016; Beddingfield and Cartwright, 2020). Thus, straight rim segments of PICs reveal hidden tectonic patterns on Vesta and Ceres, irrespective of their differences in compositions.

5. Implications for hypothesized tectonic processes

Various planetary processes that could form distinct regional and global tectonic patterns have previously been hypothesized for Ceres or Vesta. These include changes in the spin rate of both bodies (Mao and McKinnon, 2020), changes in volume on Ceres (McCord and Sotin, 2005), and true polar wander on Ceres (Tricarico, 2018) and Vesta (Matsuyama and Nimmo, 2011). Global stress distributions were derived for all of these processes, and tectonic patterns were predicted in some studies (e.g., Matsuyama and Nimmo, 2008, 2011; Tricarico, 2018).

To identify if these processes are relevant to the tectonic histories of Vesta and Ceres, we compare the tectonic patterns revealed by PICs on Vesta and Ceres to the predictions. The tectonic patterns revealed by PICs, as presented in Figs. 3 and 5, contain fracture sets of different ages. Their relative ages could be deduced if PICs were also analyzed based on their degradational stages, as has been done on Mercury (Yazıcı et al., 2024). Although a morphological assessment and cataloging of crater degradation was carried out for Ceres (Zeilnhofer and Barlow, 2021b), it has not yet been conducted for Vesta. Thus, we can compare only the preserved pattern as a whole between the two bodies in this study. Furthermore, multiple processes could have overlapped and some tectonic structures and their patterns may not be preserved, such that observations may not match the predicted patterns perfectly. Lastly, any predictions of global tectonic patterns rely on the methods and assumptions in the original studies. Therefore, the suitability of any previous predictions must be discussed in terms of fracture types and orientations and rock-mechanical properties of Vesta and Ceres.

5.1. Change in spin rate on Vesta and Ceres

Impact-induced changes in spin rate were proposed to have occurred on both Vesta and Ceres (Mao and McKinnon, 2020). Ceres is suggested to have spun up or down by one to two hours from its initial rate. Vesta may have spun up or down due to the Rheasilvia and Veneneia impacts. General studies of spin rate changes predict that a planetary spin-up produces a global tectonic pattern with normal faults trending N–S at the equatorial region, strike-slip faults trending NE–SW and NW–SE in the mid-latitudes, and thrust faults trending E–W in the pole regions (Matsuyama and Nimmo, 2008; Beuthe, 2010). In contrast, despinning is predicted to include thrust fault trending N–S at the equatorial region, strike-slip faults trending NE–SW and NW–SE in the mid-latitudes, and normal faults trending E–W in the pole regions (Melosh, 1977; Collins et al., 2010).

However, Klimczak et al. (2015) determined that despinning produced a global set of mostly E–W-oriented joints on Mercury. These authors noted that the widely used Anderson's theory of faulting (Anderson, 1951) to predict the type of faults on planetary surfaces is not appropriate, as it does not apply to tensile stresses, but that N–S oriented stress components remain tensile across all latitudes during despinning. For Mercury's low surface gravitational acceleration, tensile stresses were not shifted into a fully compressive stress state, in which Anderson's theory of faulting does apply until considerable depths are reached. Such conditions are equally applicable to bodies like Vesta and Ceres that have even lower surface gravitational accelerations than Mercury (see Cheng and Klimczak, 2022b).

While the tectonic patterns on Ceres (Fig. 5) do not fit with any of those generally predicted from changes in spin rates, some comparison is possible for Vesta. On Vesta, E–W preferred orientations at the poles, such as those predicted in general for changes in spin rates, are present in the orientations of straight crater rim segments (Fig. 3). However, no distinctive N–S trending pattern occurs in the structural observations in the equatorial region (Fig. 3). Moreover, Mao and McKinnon (2020) proposed that the extension driven by a spin-up has a role in the formation of the Divalia Fossae and perhaps even the Saturnalia Fossae. However, no studies specifically predict the type and orientation of structures resulting from changes in spin rate on Vesta (and Ceres) to make comparisons of the tectonic patterns revealed by PICs or other mapped tectonic structures. Thus, a change in spin rate on either of these bodies cannot be confirmed or ruled out.

5.2. Volume change on Ceres

Complex phases of global contraction are thought to have occurred during Ceres's evolution, and tectonic structures that formed during several stages are hypothesized to be present in the crust today (McCord and Sotin, 2005). Assuming a constant lithospheric thickness, a body

experiencing a global volume decrease is likely to have a global population of randomly oriented and uniformly distributed thrust faults. In contrast, a global volume increase, i.e., global expansion, is likely to produce randomly oriented and uniformly distributed joints and perhaps normal faults (Melosh and McKinnon, 1988). However, the observed global tectonic pattern on Ceres shows systematic changes with latitude and exhibits preferred orientations across all observed geographic regions. These observations do not match the predicted patterns of either global expansion or contraction.

Several studies suggest that Ceres has a thick lithosphere with heterogeneous crustal density (e.g., Tricarico, 2018; Park et al., 2020; Zeilhofer and Barlow, 2021a). These lithospheric heterogeneities can significantly affect tectonic patterns induced by volume changes. For instance, icy bodies with a thinner equatorial lithosphere and a thicker polar lithosphere are predicted to form E–W trending normal faults during expansion or thrust faults during contraction, particularly in the equatorial region (Beuthe, 2010). Ceres is proposed to have a lower crustal density in the north polar region compared to the equator and southern latitudes (Park et al., 2020), but what tectonic patterns would emerge from such a physical setting remains unclear.

5.3. True polar wander

Prior to the Dawn mission, tectonic patterns caused by a series of overlapping processes involving true polar wander (TPW) on Vesta were investigated (Matsuyama and Nimmo, 2011). The investigated processes involved TPW overlapping with tidal despinning and global contraction. TPW alone was found to cause complex tectonic patterns involving normal, thrust, and strike-slip faults arranged around the inferred paleopoles (see Matsuyama and Nimmo, 2011). None of the predicted patterns in Matsuyama and Nimmo (2011) match the observed orientations of PIC-forming fractures reported in this study, ruling out that the investigated specific geophysical scenarios in that study took place. However, modification of the location of paleopoles and amount of despinning as well as reassessment of fracturing behavior using rock-mechanical considerations may lead to new insights, especially given the wealth of geophysical and geological constraints that were established since the Dawn mission.

Numerical modeling of the relaxation of the Rheasilvia basin and Vesta's rotational bulge was also previously investigated to test for the possibility of TPW (Karimi and Dombard, 2016). The results therein suggest that the thickness and rigidity of Vesta's lithosphere following the impact likely inhibited any relaxation of Vesta's rotational bulge (Karimi and Dombard, 2016). However, the rigidity parameters used in this modeling pertained to those for intact rock samples and are likely not suitable for highly fractured rock masses such as those comprising Vesta's lithosphere. It remains to be tested if revised elastic lithospheric parameters that reduce the rigidity allow for basin relaxation and polar flattening to occur, and thus the possibility of TPW on Vesta cannot yet be discounted.

Ceres is also proposed to have undergone TPW caused by a heterogeneous crustal density distribution (Tricarico, 2018), in which the induced stress field could fracture the lithosphere of Ceres and contribute to the formation of PICs. Tricarico (2018) proposed a reorientation of Ceres' pole by $\sim 36^\circ$ with multiple stages of pole changes. Similar to the prediction by Matsuyama and Nimmo (2011) for Vesta described above, TPW on Ceres is predicted to have produced complex tectonic patterns involving normal and thrust faults arranged around the inferred paleopoles (see Tricarico, 2018). Our latitudinal variations of the tectonic pattern on Ceres (Fig. 5) do not match with the predicted patterns of true polar wander (TPW) proposed by Tricarico (2018). The lithosphere of Ceres is intricately fractured (Fig. 5), and although a few fracture orientations may align with the predicted tectonic structures in Tricarico (2018), it does not confirm that TPW took place. In fact, the parameter space test by Keane and Ermakov (2019) shows that tectonic patterns on Ceres are ambiguous enough that a significant portion of

random paleo-poles could result in tectonic patterns of which portions fit the observed structures. Therefore, our fracture orientations inferred from PICs do not support TPW on Ceres.

Furthermore, pit crater chains, such as Samhain Catena, were proposed to match the predicted pattern of TPW on Ceres (Tricarico, 2018). However, similar to the generally predicted tectonic pattern for despinning (e.g., Melosh, 1977; Matsuyama and Nimmo, 2008; Beuthe, 2010; Collins et al., 2010), the tectonic pattern predicted by Tricarico (2018) considered faulting as the only fracturing type induced by TPW. However, Ceres is a small and low-gravity body, where faulting is unlikely to form near the surface in the presence of tensile stresses (Cheng and Klimczak, 2022b). Jointing must also be considered in rock-mechanical reassessments to allow for rock-mechanically sound predictions of tectonic patterns and proper comparison with the observed fracture types and patterns.

6. Conclusions and future work

This work shows that PICs on Vesta and Ceres reveal hidden fracture sets. We mapped and analyzed 412 craters with a diameter larger than 10 km on Vesta and 525 craters with a diameter larger than 20 km on Ceres. A total of 73 % of mapped craters on Vesta and 100 % of mapped craters on Ceres have at least one straight rim segment and thus are categorized as PICs. By plotting the orientations of straight crater rim segments binned for several different geographic regions, we identified preferred orientations and their variations across the globe for both bodies. Vesta has a pronounced E–W oriented fracture pattern in the polar regions with several regional fracture sets intersecting one another across the globe. Ceres has many intersecting fractures with a dominant preferred NE–SW fracture set in the northern hemisphere and a dominant NW–SE fracture set in the southern hemisphere, where these patterns are most pronounced near the poles.

None of the fracture patterns revealed by straight crater rim segments conclusively match the orientations of prominent tectonic landforms on either body. Therefore, the tectonic patterns identified in our study may be formed by processes unrelated to these landforms. While Vesta and Ceres are both fast-spinning bodies, their different tectonic patterns could be accounted for by differences in crater sizes and types, surface gravitational acceleration, crustal materials, as well as a wealth of different overlapping planetary processes. We attempted to compare the tectonic patterns revealed of Vesta and Ceres with the predicted tectonic pattern caused by the change in spinning rate, volume change, and true polar wander. However, the prediction of tectonic patterns for many of the suggested processes is incomplete or not specific to Vesta and Ceres and thus does not allow for proper comparisons. A reassessment of rock-mechanical properties tailored to the lithospheres of Vesta and Ceres is necessary for more accurate predictions of tectonic patterns and to enable meaningful comparisons with observations in future studies.

CRediT authorship contribution statement

Hiu Ching Jupiter Cheng: Writing – original draft, Visualization, Methodology, Investigation, Funding acquisition, Formal analysis, Data curation, Conceptualization. **Christian Klimczak:** Writing – review & editing, Validation, Supervision, Methodology, Investigation, Conceptualization.

Declaration of competing interest

The authors declare that they have no known competing financial interests or personal relationships that could have appeared to influence the work reported in this paper.

Acknowledgments

We thank Teemu Öhman and an anonymous reviewer who provided feedback on the earlier version of this manuscript. This research was

made possible by the 2020 Eugene and Carolyn Shoemaker Impact Cratering Award. This work made use of NASA Dawn Mission data, which are archived in the NASA Planetary Data System under the Small Bodies Node.

Appendix A. Statistics for mapped craters on Vesta

Table A1

Statistics of all crater rims binned by latitudes.

Region #	Lat	Length ^a	Total % ^b	# of bins ^c	V ^d	P-value
1	60°N - 90°N	1638	12 %	24	3.0743	< 0.01
2	30°N - 60°N	3611	26 %	30	2.3484	< 0.01
3	0 - 30°N	3478	25 %	30	2.7523	< 0.01
4	30S - 0	2781	20 %	30	1.8084	0.025 < P < 0.05
5	60S - 30S	1430	10 %	24	1.1606	> 0.15
6	90S - 60S	760	6 %	18	1.4002	> 0.15

^a Total mapped crater rim length in km.

^b Percentage of mapped crater rim lengths in the region.

^c Number of bins in the rose diagram (see calculations in the main text).

^d Test statistic for Kuiper's test.

Table A2

Statistics of extracted straight rim segments binned by latitudes.

Region #	Lat	Length ^a	Total % ^b	# of bins ^c	V ^d	P-value
1	60°N - 90°N	763	13 %	18	11.3559	< 0.01
2	30°N - 60°N	1454	25 %	24	4.8351	< 0.01
3	0 - 30°N	1589	27 %	24	2.2847	< 0.01
4	30S - 0	1085	19 %	20	2.2382	< 0.01
5	60S - 30S	544	9 %	18	2.8471	< 0.01
6	90S - 60S	401	7 %	18	6.7746	< 0.01

^a Total mapped crater rim length in km.

^b Percentage of mapped crater rim lengths in the region.

^c Number of bins in the rose diagram (see calculations in the main text).

^d Test statistic for Kuiper's test.

Table A3

Statistics of all crater rims binned by longitudes.

Region #	Lon	Length ^a	Total % ^b	# of bins ^c	V ^d	P-value
7	180°W - 150°W	1341	10 %	24	1.8179	0.025 < P-value < 0.05
8	150°W - 120°W	1127	8 %	20	1.8752	0.01 < P-value < 0.025
9	120°W - 90°W	1149	8 %	20	0.986	> 0.15
10	90°W - 60°W	1426	10 %	24	1.1603	> 0.15
11	60°W - 30°W	1038	8 %	20	0.9924	> 0.15
12	30°W - 0	1446	11 %	24	1.1777	> 0.15
13	0 - 30E	1147	8 %	20	1.4165	> 0.15
14	30E - 60E	748	5 %	18	1.011	> 0.15
15	60E - 90E	1051	8 %	20	1.1563	> 0.15
16	90E - 120E	1077	8 %	20	1.0738	> 0.15
17	120E - 150E	785	6 %	18	1.5638	0.10 < P-value < 0.15
18	150E - 180E	1363	10 %	24	1.0411	> 0.15

^a Total mapped crater rim length in km.

^b Percentage of mapped crater rim lengths in the region.

^c Number of bins in the rose diagram (see calculations in the main text).

^d Test statistic for Kuiper's test.

Table A4

Statistics of extracted straight rim segments binned by longitudes.

Region #	Lon	Length ^a	Total % ^b	# of bins ^c	V ^d	P-value
7	180°W - 150°W	665	11 %	18	4.6175	< 0.01
8	150°W - 120°W	403	7 %	18	3.6928	< 0.01
9	120°W - 90°W	435	7 %	18	3.1884	< 0.01
10	90°W - 60°W	624	11 %	18	4.4393	< 0.01

(continued on next page)

Table A4 (continued)

Region #	Lon	Length ^a	Total % ^b	# of bins ^c	V ^d	P-value
11	60°W - 30°W	468	8 %	18	2.539	< 0.01
12	30°W - 0	737	13 %	18	3.6182	< 0.01
13	0 - 30E	386	7 %	18	2.8734	< 0.01
14	30E - 60E	281	5 %	12	2.1053	< 0.01
15	60E - 90E	483	8 %	18	3.8266	< 0.01
16	90E - 120E	466	8 %	18	3.4086	< 0.01
17	120E - 150E	302	5 %	12	2.7783	< 0.01
18	150E - 180E	583	10 %	18	3.3627	< 0.01

^a Total mapped crater rim length in km.^b Percentage of mapped crater rim lengths in the region.^c Number of bins in the rose diagram (see calculations in the main text).^d Test statistic for Kuiper's test.**Table A5**

Statistics of all crater rims binned by 18 global regions.

Region #	Lat	Lon	Length ^a	Total % ^b	# of bins ^c	V ^d	P-value
19	60°N - 90°N	ALL	1638	12 %	24	3.0743	< 0.01
20	30°N - 60°N	180 - 60°W	1330	10 %	24	1.3339	> 0.15
21	30°N - 60°N	60°W - 60E	1069	8 %	20	1.2447	> 0.15
22	30°N - 60°N	60E - 180	1212	9 %	20	2.033	< 0.01
23	0 - 30°N	180 - 108°W	1073	8 %	20	2.6142	< 0.01
24	0 - 30°N	108°W - 36°W	601	4 %	18	1.9438	0.01 < P-value < 0.025
25	0 - 30°N	36°W - 36E	688	5 %	18	1.6604	0.05 < P-value < 0.10
26	0 - 30°N	36E - 108 E	442	3 %	15	1.3787	> 0.15
27	0 - 30°N	108E - 180	674	5 %	18	1.069	> 0.15
28	30S - 0	180 - 108°W	464	3 %	15	1.2003	> 0.15
29	30S - 0	108°W - 36°W	743	5 %	18	1.5789	0.10 < P-value < 0.15
30	30S - 0	36°W - 36E	674	5 %	18	1.031	> 0.15
31	30S - 0	36E - 108 E	485	4 %	15	1.183	> 0.15
32	30S - 0	108E - 180	415	3 %	15	1.1823	> 0.15
33	60S - 30S	180 - 60°W	532	4 %	18	1.1019	> 0.15
34	60S - 30S	60°W - 60E	445	3 %	15	0.7679	> 0.15
35	60S - 30S	60E - 180	453	3 %	15	1.1146	> 0.15
36	90S - 60S	ALL	760	6 %	18	1.4002	> 0.15

^a Total mapped crater rim length in km.^b Percentage of mapped crater rim lengths in the region.^c Number of bins in the rose diagram (see calculations in the main text).^d Test statistic for Kuiper's test.**Table A6**

Statistics of extracted straight rim segments binned by 18 regions.

Region #	Lat	Lon	Length ^a	Total % ^b	# of bins ^c	V ^d	P-value
19	60°N - 90°N	ALL	763	13 %	18	11.356	< 0.01
20	30°N - 60°N	180 - 60°W	556	10 %	18	3.494	< 0.01
21	30°N - 60°N	60°W - 60E	461	8 %	18	3.5749	< 0.01
22	30°N - 60°N	60E - 180	436	7 %	18	3.0269	< 0.01
23	0 - 30°N	180 - 108°W	436	7 %	18	3.1152	< 0.01
24	0 - 30°N	108°W - 36°W	211	4 %	12	2.323	< 0.01
25	0 - 30°N	36°W - 36E	383	7 %	18	1.7867	0.025 < P-value < 0.05
26	0 - 30°N	36E - 108 E	246	4 %	12	1.8818	0.01 < P-value < 0.025
27	0 - 30°N	108E - 180	310	5 %	12	1.9523	0.01 < P-value < 0.025
28	30S - 0	180 - 108°W	149	3 %	12	2.8751	< 0.01
29	30S - 0	108°W - 36°W	286	5 %	12	1.7934	< P-value < 0.05
30	30S - 0	36°W - 36E	243	4 %	12	2.7693	< 0.01
31	30S - 0	36E - 108 E	232	4 %	12	1.8405	0.025 < P-value < 0.05
32	30S - 0	108E - 180	172	3 %	12	1.8191	0.025 < P-value < 0.05
33	60S - 30S	180 - 60°W	237	4 %	12	2.9545	< 0.01
34	60S - 30S	60°W - 60E	139	2 %	10	2.5533	< 0.01
35	60S - 30S	60E - 180	167	3 %	12	1.5993	0.10 < P-value < 0.15
36	90S - 60S	ALL	401	7 %	18	6.7746	< 0.01

^a Total mapped crater rim length in km.^b Percentage of mapped crater rim lengths in the region.^c Number of bins in the rose diagram (see calculations in the main text).^d Test statistic for Kuiper's test.

Table A7

Statistics of all crater rims binned by 18 regions from the center of Rheasilvia basin.

Region #	Lat	Lon	Length ^a	Total % ^b	# of bins ^c	V ^d	P-value
1	60°N - 90°N	ALL	700	5 %	18	1.11	> 0.15
2	30°N - 60°N	180 - 60°W	540	4 %	18	1.346	> 0.15
3	30°N - 60°N	60°W - 60E	437	3 %	18	1.0962	> 0.15
4	30°N - 60°N	60E - 180	295	2 %	12	0.8566	> 0.15
5	0 - 30°N	180 - 108°W	564	4 %	18	1.3835	> 0.15
6	0 - 30°N	108°W - 36°W	536	4 %	18	1.0411	> 0.15
7	0 - 30°N	36°W - 36E	517	4 %	18	0.7986	> 0.15
8	0 - 30°N	36E - 108 E	793	6 %	18	1.1981	> 0.15
9	0 - 30°N	108E - 180	519	4 %	18	1.9201	0.01 < P-value < 0.025
10	30S - 0	180 - 108°W	946	7 %	18	1.6369	0.05 < P-value < 0.10
11	30S - 0	108°W - 36°W	740	5 %	18	1.9467	0.01 < P-value < 0.025
12	30S - 0	36°W - 36E	609	4 %	18	1.8158	0.025 < P-value < 0.05
13	30S - 0	36E - 108 E	710	5 %	18	1.5728	0.10 < P-value < 0.15
14	30S - 0	108E - 180	626	5 %	18	1.1363	> 0.15
15	60S - 30S	180 - 60°W	1138	8 %	20	2.1525	< 0.01
16	60S - 30S	60°W - 60E	1132	8 %	20	1.5358	> 0.15
17	60S - 30S	60E - 180	1194	9 %	20	2.2914	< 0.01
18	90S - 60S	ALL	1702	12 %	24	1.9831	0.01 < P-value < 0.025

^a Total mapped crater rim length in km.^b Percentage of mapped crater rim lengths in the region.^c Number of bins in the rose diagram (see calculations in the main text).^d Test statistic for Kuiper's test.**Table A8**

Statistics of extracted straight rim segments binned by 18 regions from the center of Rheasilvia basin.

Region #	Lat	Lon	Length ^a	Total % ^b	# of bins ^c	V ^d	P-value
1	60°N - 90°N	ALL	317	5 %	12	4.8625	< 0.01
2	30°N - 60°N	180 - 60°W	230	4 %	12	2.5043	< 0.01
3	30°N - 60°N	60°W - 60E	211	4 %	12	4.487	< 0.01
4	30°N - 60°N	60E - 180	85	1 %	10	2.1615	< 0.01
5	0 - 30°N	180 - 108°W	207	4 %	12	1.6992	0.05 < P-value < 0.10
6	0 - 30°N	108°W - 36°W	173	3 %	12	2.7792	< 0.01
7	0 - 30°N	36°W - 36E	233	4 %	12	1.5365	> 0.15
8	0 - 30°N	36E - 108 E	339	6 %	12	2.3731	< 0.01
9	0 - 30°N	108E - 180	277	5 %	12	2.8181	< 0.01
10	30S - 0	180 - 108°W	465	8 %	18	2.2696	< 0.01
11	30S - 0	108°W - 36°W	326	6 %	12	2.7512	< 0.01
12	30S - 0	36°W - 36E	210	4 %	12	1.7954	0.01 < P-value < 0.025
13	30S - 0	36E - 108 E	328	6 %	12	2.1478	< 0.01
14	30S - 0	108E - 180	250	4 %	12	1.6663	0.10 < P-value < 0.15
15	60S - 30S	180 - 60°W	380	7 %	18	4.7307	< 0.01
16	60S - 30S	60°W - 60E	498	9 %	18	2.5235	< 0.01
17	60S - 30S	60E - 180	529	9 %	18	6.0582	< 0.01
18	90S - 60S	ALL	774.1785517	13 %	18	7.5653	< 0.01

^a Total mapped crater rim length in km.^b Percentage of mapped crater rim lengths in the region.^c Number of bins in the rose diagram (see calculations in the main text).^d Test statistic for Kuiper's test.

Appendix B. Statistics for mapped craters on Ceres

Table B1

Statistics of all crater rims binned by latitudes.

Region #	Lat	Length ^a	Total % ^b	# of bins ^c	V ^d	P-value
1	60°N - 90°N	4058	10 %	30	5.57	< 0.01
2	30°N - 60°N	9923	25 %	36	4.7947	< 0.01
3	0 - 30°N	9678	25 %	36	6.0365	< 0.01
4	30S - 0	7067	18 %	36	4.3931	< 0.01
5	60S - 30S	5908	15 %	36	5.8524	< 0.01
6	90S - 60S	2669	7 %	30	4.6199	< 0.01

^a Total mapped crater rim length in km.^b Percentage of mapped crater rim lengths in the region.^c Number of bins in the rose diagram (see calculations in the main text).^d Test statistic for Kuiper's test.

Table B2

Statistics of extracted straight rim segments binned by latitudes.

Region #	Lat	Length ^a	Total % ^b	# of bins ^c	V ^d	P-value
1	60°N - 90°N	1638	12 %	24	3.0743	< 0.01
2	30°N - 60°N	3611	26 %	30	2.3484	< 0.01
3	0 - 30°N	3478	25 %	30	2.7523	< 0.01
4	30S - 0	2781	20 %	30	1.8084	0.025 < P-value < 0.05
5	60S - 30S	1430	10 %	24	1.1606	> 0.15
6	90S - 60S	760	6 %	18	1.4002	> 0.15

^a Total mapped crater rim length in km.^b Percentage of mapped crater rim lengths in the region.^c Number of bins in the rose diagram (see calculations in the main text).^d Test statistic for Kuiper's test.**Table B3**

Statistics of all crater rims binned by longitudes.

Region #	Lon	Length ^a	Total % ^b	# of bins ^c	V ^d	P-value
7	180°W - 150°W	4855	12 %	36	2.699	< 0.01
8	150°W - 120°W	3599	9 %	30	2.2982	< 0.01
9	120°W - 90°W	2904	7 %	30	3.0117	< 0.01
10	90°W - 60°W	3134	8 %	30	2.1374	< 0.01
11	60°W - 30°W	2897	7 %	30	2.5721	< 0.01
12	30°W - 0	2988	8 %	30	1.9001	0.01 < P-value < 0.025
13	0 - 30E	2938	7 %	30	1.7071	0.05 < P-value < 0.10
14	30E - 60E	3397	9 %	30	2.2768	< 0.01
15	60E - 90E	2694	7 %	30	2.1445	< 0.01
16	90E - 120E	2586	7 %	30	2.6747	< 0.01
17	120E - 150E	3510	9 %	30	4.0474	< 0.01
18	150E - 180E	3798	10 %	30	2.2552	< 0.01

^a Total mapped crater rim length in km.^b Percentage of mapped crater rim lengths in the region.^c Number of bins in the rose diagram (see calculations in the main text).^d Test statistic for Kuiper's test.**Table B4**

Statistics of extracted straight rim segments binned by longitudes.

Region #	Lon	Length ^a	Total % ^b	# of bins ^c	V ^d	P-value
7	180°W - 150°W	1341	10 %	24	1.8179	0.025 < P-value < 0.05
8	150°W - 120°W	1127	8 %	20	1.8752	0.01 < P-value < 0.025
9	120°W - 90°W	1149	8 %	20	0.986	> 0.15
10	90°W - 60°W	1426	10 %	24	1.1603	> 0.15
11	60°W - 30°W	1038	8 %	20	0.9924	> 0.15
12	30°W - 0	1446	11 %	24	1.1777	> 0.15
13	0 - 30E	1147	8 %	20	1.4165	> 0.15
14	30E - 60E	748	5 %	18	1.011	> 0.15
15	60E - 90E	1051	8 %	20	1.1563	> 0.15
16	90E - 120E	1077	8 %	20	1.0738	> 0.15
17	120E - 150E	785	6 %	18	1.5638	0.10 < P-value < 0.15
18	150E - 180E	1363	10 %	24	1.0411	> 0.15

^a Total mapped crater rim length in km.^b Percentage of mapped crater rim lengths in the region.^c Number of bins in the rose diagram (see calculations in the main text).^d Test statistic for Kuiper's test.**Table B5**

Statistics of all crater rims binned by 18 global regions.

Region #	Lat	Lon	Length ^a	Total % ^b	# of bins ^c	V ^d	P-value
19	60°N - 90°N	ALL	4058	10 %	30	5.57	< 0.01
20	30°N - 60°N	180 - 60°W	3981	10 %	30	2.7884	< 0.01
21	30°N - 60°N	60°W - 60E	3200	8 %	30	3.4891	< 0.01
22	30°N - 60°N	60E - 180	2742	7 %	30	4.5204	< 0.01
23	0 - 30°N	180 - 108°W	2393	6 %	24	3.4898	< 0.01
24	0 - 30°N	108°W - 36°W	1856	5 %	24	3.4614	< 0.01
25	0 - 30°N	36°W - 36E	1617	4 %	24	3.1868	< 0.01
26	0 - 30°N	36E - 108 E	1923	5 %	24	3.1826	< 0.01
27	0 - 30°N	108E - 180	1887	5 %	24	2.7744	< 0.01
28	30S - 0	180 - 108°W	2103	5 %	24	3.7472	< 0.01

(continued on next page)

Table B5 (continued)

Region #	Lat	Lon	Length ^a	Total % ^b	# of bins ^c	V ^d	P-value
29	30S - 0	108°W - 36°W	950	2 %	20	2.7969	< 0.01
30	30S - 0	36°W - 36E	1596	4 %	24	3.0847	< 0.01
31	30S - 0	36E - 108 E	951	2 %	20	2.4685	< 0.01
32	30S - 0	108E - 180	1465	4 %	24	2.341	< 0.01
33	60S - 30S	180 - 60°W	2023	5 %	24	3.391	< 0.01
34	60S - 30S	60°W - 60E	1501	4 %	24	3.3147	< 0.01
35	60S - 30S	60E - 180	2382	6 %	24	4.3499	< 0.01
36	90S - 60S	ALL	2669	7 %	30	4.6199	< 0.01

^a Total mapped crater rim length in km.^b Percentage of mapped crater rim lengths in the region.^c Number of bins in the rose diagram (see calculations in the main text).^d Test statistic for Kuiper's test.**Table B6**

Statistics of extracted straight rim segments binned by 18 global regions.

Region #	Lat	Lon	Length ^a	Total % ^b	# of bins ^c	V ^d	P-value
19	60°N - 90°N	ALL	1638	12 %	24	3.0743	< 0.01
20	30°N - 60°N	180 - 60°W	1330	10 %	24	1.3339	> 0.15
21	30°N - 60°N	60°W - 60E	1069	8 %	20	1.2447	> 0.15
22	30°N - 60°N	60E - 180	1212	9 %	20	2.033	< 0.01
23	0 - 30°N	180 - 108°W	1073	8 %	20	2.6142	< 0.01
24	0 - 30°N	108°W - 36°W	601	4 %	18	1.9438	0.01 < P-value < 0.025
25	0 - 30°N	36°W - 36E	688	5 %	18	1.6604	0.05 < P-value < 0.10
26	0 - 30°N	36E - 108 E	442	3 %	15	1.3787	> 0.15
27	0 - 30°N	108E - 180	674	5 %	18	1.069	> 0.15
28	30S - 0	180 - 108°W	464	3 %	15	1.2003	> 0.15
29	30S - 0	108°W - 36°W	743	5 %	18	1.5789	0.10 < P-value < 0.15
30	30S - 0	36°W - 36E	674	5 %	18	1.031	> 0.15
31	30S - 0	36E - 108 E	485	4 %	15	1.183	> 0.15
32	30S - 0	108E - 180	415	3 %	15	1.1823	> 0.15
33	60S - 30S	180 - 60°W	532	4 %	18	1.1019	> 0.15
34	60S - 30S	60°W - 60E	445	3 %	15	0.7679	> 0.15
35	60S - 30S	60E - 180	453	3 %	15	1.1146	> 0.15
36	90S - 60S	ALL	760	6 %	18	1.4002	> 0.15

^a Total mapped crater rim length in km.^b Percentage of mapped crater rim lengths in the region.^c Number of bins in the rose diagram (see calculations in the main text).^d Test statistic for Kuiper's test.

Appendix C. Supplementary data

Supplementary data to this article can be found online at <https://doi.org/10.1016/j.icarus.2025.116528>.

Data availability

We have shared a link to the data used in the manuscript in Appendix C.

References

- Aittola, M., Öhman, T., Leitner, J.J., Raitala, J., 2007. The characteristics of polygonal impact craters on Venus. *Earth Moon Planet.* 101, 41–53. <https://doi.org/10.1007/s11038-007-9148-4>.
- Aittola, M., Öhman, T., Leitner, J.J., Kostama, V.P., Raitala, J., 2010. The structural control of Venusian polygonal impact craters. *Icarus* 205 (2), 356–363. <https://doi.org/10.1016/j.icarus.2009.08.004>.
- Ammannito, E., DeSanctis, M.C., Ciarniello, M., Frigeri, A., Carrozzo, F.G., Combe, J.P., Ehmann, B.L., Marchi, S., McSween, H.Y., Raponi, A., Toplis, M.J., 2016. Distribution of phyllosilicates on the surface of Ceres. *Science* 353 (6303), aaf4279. <https://doi.org/10.1126/science.aaf4279>.
- Anderson, E.M., 1951. *The Dynamics of Faulting, Etc.(Revised.)*. Edinburgh, London.
- Asphaug, E., Moore, J.M., Morrison, D., Benz, W., Nolan, M.C., Sullivan, R.J., 1996. Mechanical and geological effects of impact cratering on Ida. *Icarus* 120 (1), 158–184.
- Baby, N.R., Kenkmann, T., Stephan, K., Wagner, R., 2024. Polygonal impact craters on Ganymede. *Meteorit. Planet. Sci.* 59 (3), 544–559. <https://doi.org/10.1111/maps.14138>.
- Baldwin, R.B., 1963. *The Measure of the Moon*. University Chicago Press, Chicago, p. 128.
- Beddingfield, C.B., Cartwright, R.J., 2020. Hidden tectonism on Miranda's Elsinore Corona revealed by polygonal impact craters. *Icarus* 343, 113687. <https://doi.org/10.1016/j.icarus.2020.113687>.
- Beddingfield, C.B., Burr, D.M., Tran, L.T., 2016. Polygonal impact craters on Dione: evidence for tectonic structures outside the wispy terrain. *Icarus* 274, 163–194. <https://doi.org/10.1016/j.icarus.2016.03.020>.
- Beddingfield, C.B., Crane, K., Klimczak, C., Cartwright, R., 2024. Mercury's lobate scarps reveal that polygonal impact craters form on Contractual structures. *Planet. Sci. J.* 5 (2), 52.
- Beuthe, M., 2010. East–west faults due to planetary contraction. *Icarus* 209 (2), 795–817. <https://doi.org/10.1016/j.icarus.2010.04.019>.
- Binder, A.B., McCarthy Jr., D.W., 1972. Mars: the lineament systems. *Science* 176 (4032), 279–281. <https://doi.org/10.1126/science.176.4032.279>.
- Buczkowski, D.L., Schmidt, B.E., Williams, D.A., Mest, S.C., Scully, J.E.C., Ermakov, A.I., Preusker, F., Schenk, P., Otto, K.A., Hiesinger, H., O'Brien, D., 2016. The geomorphology of Ceres. *Science* 353 (6303). <https://doi.org/10.1126/science.aaf4332> p. aaf4332.
- Buczkowski, D.L., Wyrick, D.Y., Iyer, K.A., Kahn, E.G., Scully, J.E.C., Nathues, A., Gaskell, R.W., Roatsch, T., Preusker, F., Schenk, P.M., Le Corre, L., 2012. Large-scale troughs on Vesta: A signature of planetary tectonics. *Geophysical Research Letters* 39 (18). <https://doi.org/10.1029/2012GL052959>.
- Byrne, P.K., Klimczak, C., Celal Şengör, A.M., Solomon, S.C., Watters, T.R., Hauck II, S. A., 2014. Mercury's global contraction much greater than earlier estimates. *Nat. Geosci.* 7 (4), 301–307.
- Carr, M.H., Crumpler, L.S., Cutts, J.A., Greeley, R., Guest, J.E., Masursky, H., 1977. Martian impact craters and emplacement of ejecta by surface flow. *J. Geophys. Res.* 82 (28), 4055–4065.

- Castillo-Rogez, J., Neveu, M., McSween, H.Y., Fu, R.R., Toplis, M.J., Prettyman, T., 2018. Insights into Ceres's evolution from surface composition. *Meteorit. Planet. Sci.* 53 (9), 1820–1843. <https://doi.org/10.1111/maps.13181>.
- Cheng, H.C.J., 2024. Tectonic patterns on Vesta and Ceres revealed by polygonal impact craters. Mendeley Data VI. <https://doi.org/10.17632/ynvy7nvp5m.1>.
- Cheng, H.C.J., Klimczak, C., 2022a. Structural relationships in and around the Rheasilvia basin on Vesta. *J. Struct. Geol.* 161, 104677. <https://doi.org/10.1016/j.jsg.2022.104677>.
- Cheng, H.C.J., Klimczak, C., 2022b. Large-scale troughs on asteroid 4 Vesta accommodate opening-mode displacement. *J. Geophys. Res. Planets* 127 (6). <https://doi.org/10.1029/2021JE007130> p. e2021JE007130.
- Collins, G.C., McKinnon, W.B., Moore, J.M., Nimmo, F., Pappalardo, R.T., Prockter, L.M., Schenk, P.M., 2010. Tectonics of the outer planet satellites. In: Watters, T.R., Schultz, R.A. (Eds.), *Planetary Tectonics*: New York. Cambridge University Press, pp. 264–350.
- Dasgupta, D., Kundu, A., De, K., Dasgupta, N., 2019. Polygonal impact craters in the Thaumasia Minor, Mars: role of pre-existing faults in their formation. *J. Indian Soc. Remote Sensing* 47, 257–265.
- Eppler, D.T., Ehrlich, R., Nummedal, D., Schultz, P.H., 1983. Sources of shape variation in lunar impact craters: Fourier shape analysis. *Geol. Soc. Am. Bull.* 94 (2), 274–291.
- Freedman, D., Diaconis, P., 1981. On the histogram as a density estimator: L 2 theory. *Zeitschrift für Wahrscheinlichkeitstheorie und verwandte Gebiete* 57 (4), 453–476.
- Hiesinger, H., Marchi, S., Schmedemann, N., Schenk, P., Pasckert, J.H., Neesemann, A., O'Brien, D.P., Kneissl, T., Ermakov, A.I., Fu, R.R., Bland, M.T., 2016. Cratering on Ceres: implications for its crust and evolution. *Science* 353 (6303), aaf4759. <https://doi.org/10.1126/science.aaf4759>.
- Jaumann, R., Williams, D.A., Buczkowski, D.L., Yingst, R.A., Preusker, F., Hiesinger, H., Schmedemann, N., Kneissl, T., Vincent, J.B., Blewett, D.T., Buratti, B.J., 2012. Vesta's shape and morphology. *Science* 336 (6082), 687–690. <https://doi.org/10.1126/science.121912>.
- Jenness, J., 2011. Tools for Graphics and Shapes. Jenness Enterprises.
- Karimi, S., Dombard, A.J., 2016. On the possibility of viscoelastic deformation of the large south polar craters and true polar wander on the asteroid Vesta. *J. Geophys. Res. Planets* 121 (9), 1786–1797.
- Keane, J.T., Ermakov, A.I., 2019. No evidence for true polar wander of Ceres. *Nat. Geosci.* 12 (12), 972–974. <https://doi.org/10.1038/s41561-018-0232-3>.
- Klimczak, C., Byrne, P.K., Solomon, S.C., 2015. A rock-mechanical assessment of Mercury's global tectonic fabric. *Earth Planet. Sci. Lett.* 416, 82–90.
- Konopliv, A.S., Park, R.S., Vaughan, A.T., Bills, B.G., Asmar, S.W., Ermakov, A.I., Rambaux, N., Raymond, C.A., Castillo-Rogez, J.C., Russell, C.T., Smith, D.E., 2018. The Ceres gravity field, spin pole, rotation period and orbit from the Dawn radiometric tracking and optical data. *Icarus* 299, 411–429. <https://doi.org/10.1016/j.icarus.2017.08.005>.
- Krishna, N., Kumar, P.S., 2016. Impact spallation processes on the moon: a case study from the size and shape analysis of ejecta boulders and secondary craters of Censorinus crater. *Icarus* 264, 274–299. <https://doi.org/10.1016/j.icarus.2015.09.033>.
- Kuiper, N.H., 1960. On the random cumulative frequency function. *Indag. Math.* 22, 32–37.
- Kumar, P.S., Kring, D.A., 2008. Impact fracturing and structural modification of sedimentary rocks at meteor crater, Arizona. *J. Geophys. Res. Planets* 113 (E9), E09009. <https://doi.org/10.1029/2008JE003115>.
- Liu, Z., Yue, Z., Michael, G., Gou, S., Di, K., Sun, S., Liu, J., 2018. A global database and statistical analyses of (4) Vesta craters. *Icarus* 311, 242–257. <https://doi.org/10.1016/j.icarus.2018.04.006>.
- Mao, X., McKinnon, W.B., 2020. Spin evolution of Vesta and Ceres due to impacts. *Meteorit. Planet. Sci.* 55 (11), 2493–2518. <https://doi.org/10.1111/maps.13594>.
- Marchi, S., McSween, H.Y., O'Brien, D.P., Schenk, P., De Sanctis, M.C., Gaskell, R., Jaumann, R., Mottola, S., Preusker, F., Raymond, C.A., Roatsch, T., 2012. The violent collisional history of asteroid 4 Vesta. *Science* 336 (6082), 690–694. <https://doi.org/10.1126/science.1218757>.
- Marchi, S., Ermakov, A.I., Raymond, C.A., Fu, R.R., O'Brien, D.P., Bland, M.T., Ammannito, E., De Sanctis, M.C., Bowling, T., Schenk, P., Scully, J.E.C., Buczkowski, D.L., Williams, D.A., Hiesinger, H., Russell, C.T., 2016. The missing large impact craters on Ceres. *Nat. Commun.* 7 (1), 12257. <https://doi.org/10.1038/ncomms12257>.
- Matsuyma, I., Nimmo, F., 2008. Tectonic patterns on reoriented and despun planetary bodies. *Icarus* 195 (1), 459–473. <https://doi.org/10.1016/j.icarus.2007.12.003>.
- Matsuyma, I., Nimmo, F., 2011. Reorientation of Vesta: gravity and tectonic predictions. *Geophys. Res. Lett.* 38 (14). <https://doi.org/10.1029/2011GL047967>.
- McCord, T.B., Scully, J.E., 2015. The composition of Vesta from the Dawn mission. *Icarus* 259, 1–9. <https://doi.org/10.1016/j.icarus.2015.03.022>.
- McCord, T.B., Sotin, C., 2005. Ceres: evolution and current state. *J. Geophys. Res. Planets* 110 (E5). <https://doi.org/10.1029/2004JE002244>.
- Melosh, H.J., 1976. Global tectonics of a despun planet. *Icarus* 31 (2), 221–243.
- Melosh, H.J., McKinnon, W.B., 1988. The tectonics of Mercury. In: *Mercury*. University of Arizona Press, pp. 374–400.
- Moore, J.M., Schenk, P.M., Bruesch, L.S., Asphaug, E., McKinnon, W.B., 2004. Large impact features on middle-sized icy satellites. *Icarus* 171 (2), 421–443.
- Neidhart, T., Leitner, J., Firneis, M., 2017. Polygonal impact craters on selected minor bodies: rhea, dione, tethys, ceres, and vesta. In: *EGU General Assembly Conference Abstracts*, p. 10081.
- Öhman, T., 2009. The Structural Control of Polygonal Impact Craters. Ph.D. Thesis. University of Oulu.
- Öhman, T., Aittola, M., Kostama, V.P., Raitala, J., 2005. The preliminary analysis of polygonal impact craters within greater Hellas region, Mars. *Impact tectonics* 131–160.
- Öhman, T., Aittola, M., Kostama, V.P., Hyvärinen, M., Raitala, J., 2006. Polygonal impact craters in the Argyre region, Mars: evidence for influence of target structure on the final crater morphology. *Meteorit. Planet. Sci.* 41 (8), 1163–1173.
- Öhman, T., Aittola, M., Kostama, V.P., Raitala, J., Korteniemi, J., 2008. Polygonal impact craters in Argyre region, Mars: implications for geology and cratering mechanics. *Meteorit. Planet. Sci.* 43 (10), 1605–1628.
- Öhman, T., Aittola, M., Korteniemi, J., Kostama, V.P., Raitala, J., 2010. Polygonal impact crater in the solar system: observations and implications. *Spec. Pap. Geol. Soc. Am.* 465, 51–65. [https://doi.org/10.1130/2010.2465\(04\)](https://doi.org/10.1130/2010.2465(04)).
- Osinski, G.R., Spray, J.G., 2005. Tectonics of complex crater formation as revealed by the Haughton impact structure, Devon Island, Canadian high Arctic. *Meteorit. Planet. Sci.* 40 (12), 1813–1834. <https://doi.org/10.1111/j.1945-5100.2005.tb00148.x>.
- Otto, K.A., Jaumann, R., Krohn, K., Buczkowski, D., Von der Gathen, I., Kersten, E., Mest, S., Nab, A., Neesemann, A., Schulz, F., Preusker, F., 2016. Origin and distribution of polygonal craters on (1) Ceres. In: *Lunar and Planetary Science Conference*, 47. Abstract 1493.
- Parekh, R., Otto, K.A., Jaumann, R., Matz, K.D., Roatsch, T., Kersten, E., Raymond, C., 2021. Influence of volatiles on mass wasting processes on Vesta and Ceres. *J. Geophys. Res. Planets* 126 (3). <https://doi.org/10.1029/2020JE006573>.
- Park, R.S., Konopliv, A.S., Ermakov, A.I., Castillo-Rogez, J.C., Fu, R.R., Hughson, K.H.G., Prettyman, T.H., Raymond, C.A., Scully, J.E.C., Sizemore, H.G., Sori, M.M., 2020. Evidence of non-uniform crust of Ceres from Dawn's high-resolution gravity data. *Nature Astronomy* 4 (8), 748–755.
- Poelchau, M.H., Kenkmann, T., Kring, D.A., 2009. Rim uplift and crater shape in meteor crater: effects of target heterogeneities and trajectory obliquity. *J. Geophys. Res. Planets* 114, E01006. <https://doi.org/10.1029/2008JE003235>.
- Prettyman, T.H., Yamashita, N., Toplis, M.J., McSween, H.Y., Schorghofer, N., Marchi, S., Feldman, W.C., Castillo-Rogez, J., Forni, O., Lawrence, D.J., Ammannito, E., Ehlmann, B.L., Sizemore, H.G., Joy, S.P., Polanskey, C.A., Rayman, M.D., Raymond, C.A., Russell, C.T., 2017. Extensive water ice within Ceres' aqueously altered regolith: evidence from nuclear spectroscopy. *Science* 355 (6320), 55–59.
- Preusker, F., Scholten, F., Matz, K.D., Roatsch, T., Jaumann, R., Raymond, C.A., Russell, C.T., 2016a. DAWN FC2 Derived Vesta DTM SPG V1.0. NASA Planetary Data System, DAWN-A.
- Preusker, F., Scholten, F., Matz, K.D., Elgner, S., Jaumann, R., Roatsch, T., Joy, S.P., Polanskey, C.A., Raymond, C.A., Russell, C.T., 2016b. Dawn at Ceres - shape model and rotational state. In: *Lunar and Planetary Science Conference*, 47. Abstract 1954.
- Prockter, L., Thomas, P., Robinson, M., Joseph, J., Milne, A., Bussey, B., Iverka, J., Cheng, A., 2002. Surface expressions of structural features on Eros. *Icarus* 155 (1), 75–93. <https://doi.org/10.1006/icar.2001.6770>.
- R Core Team, 2022. R: A Language and Environment for Statistical Computing. R Foundation for Statistical Computing, Vienna.
- Roatsch, T., Kersten, E., Matz, K.D., Preusker, F., Scholten, F., Elgner, S., Jaumann, R., Raymond, C.A., Russell, C.T., 2013. High-resolution Vesta low altitude mapping orbit atlas derived from Dawn framing camera images. *Planet. Space Sci.* 85, 293–298.
- Roatsch, T., Kersten, E., Matz, K.D., Preusker, F., Scholten, F., Jaumann, R., Raymond, C.A., Russell, C.T., 2016. High-resolution Ceres high altitude mapping orbit atlas derived from Dawn framing camera images. *Planet. Space Sci.* 129, 103–107.
- Robbins, S.J., Riggs, J.D., 2023. What is a polygonal impact crater? A proposed framework toward quantifying crater shapes. *Earth Space Sci.* 10 (7). <https://doi.org/10.1029/2023EA002863> p. e2023EA002863.
- Ruesch, O., Hiesinger, H., Blewett, D.T., Williams, D.A., Buczkowski, D., Scully, J., Yingst, R.A., Roatsch, T., Preusker, F., Jaumann, R., Russell, C.T., 2014. Geologic map of the northern hemisphere of Vesta based on Dawn framing camera (FC) images. *Icarus* 244, 41–59. <https://doi.org/10.1016/j.icarus.2014.01.035>.
- Russell, C.T., Raymond, C.A., 2011. The dawn mission to Vesta and Ceres. In: *The Dawn Mission to Minor Planets 4 Vesta and 1 Ceres*. Springer, New York, NY, pp. 3–23.
- Sanderson, D.J., Peacock, D.C., 2020. Making rose diagrams fit-for-purpose. *Earth Sci. Rev.* 201, 103055. <https://doi.org/10.1016/j.earscirev.2019.103055>.
- Schenk, P., O'Brien, D.P., Marchi, S., Gaskell, R., Preusker, F., Roatsch, T., Jaumann, R., Buczkowski, D., McCord, T., McSween, H.Y., Williams, D., 2012. The geologically recent giant impact basins at Vesta's south pole. *Science* 336 (6082), 694–697. <https://doi.org/10.1126/science.1223272>.
- Schenk, P., Castillo-Rogez, J., Otto, K.A., Marchi, S., O'Brien, D., Bland, M., Hughson, K., Schmidt, B., Scully, J., Buczkowski, D., Krohn, K., 2021. Compositional control on impact crater formation on mid-sized planetary bodies: Dawn at Ceres and Vesta, Cassini at Saturn. *Icarus* 359, 114343. <https://doi.org/10.1016/j.icarus.2021.114343>.
- Schultz, P.H., 1976. Floor-fractured lunar craters. *The Moon* 15 (3), 241–273.
- Scully, J.E., Buczkowski, D.L., Schmedemann, N., Raymond, C.A., Castillo-Rogez, J.C., King, S.D., Bland, M.T., Ermakov, A.I., O'Brien, D.P., Marchi, S., Longobardo, A.N., Russell, C.T., Fu, R.R., Neveu, M., 2017. Evidence for the interior evolution of Ceres from geologic analysis of fractures. *Geophys. Res. Lett.* 44 (19), 9564–9572. <https://doi.org/10.1002/2017GL075086>.
- Shoemaker, E.M., 1960. Impact Mechanics at Meteor Crater, Arizona. Ph.D. thesis. Princeton University.
- Shoemaker, E.M., 1962. Interpretation of lunar craters. *Phys. Astronom. Moon* 283–359.
- Siers, H., Keller, H.U., Jaumann, R., Michalik, H., Behnke, T., Bubenhausen, F., Büttner, I., Cersenty, U., Christensen, U., Enge, R., Fiethe, B., Gutierrez Marques, P., Hartwig, H., Krüger, H., Kühne, W., Maue, T., Mottola, S., Nathues, A., Reiche, K.U.,

- Richards, M.L., Roatsch, T., Schröder, S.E., Szemerey, I., Tschentscher, M., 2011. The Dawn framing camera. *Space Sci. Rev.* 163 (1), 263–327.
- Tabares-Rodenas, P., Ormö, J., Kring Jr., D.T., 2013. Cosmic wabi-sabi: tell-tale morphological imperfections in impact crater shapes revealed by numerical analysis. *Earth Planet. Sci. Lett.* 377, 211–217. <https://doi.org/10.1016/j.epsl.2013.06.043>.
- Thomas, P.C., Prockter, L.M., 2010. Tectonics of small bodies. *Planetary Tectonics* 11, 233.
- Tricarico, P., 2018. True polar wander of Ceres due to heterogeneous crustal density. *Nat. Geosci.* 11 (11), 819–824. <https://doi.org/10.1038/s41561-018-0232-3>.
- Watters, W.A., Grotzinger, J.P., Bell III, J., Grant, J., Hayes, A.G., Li, R., Squyres, S.W., Zuber, M.T., 2011. Origin of the structure and planform of small impact craters in fractured targets: endurance crater at Meridiani Planum, Mars. *Icarus* 211 (1), 472–497. <https://doi.org/10.1016/j.icarus.2010.08.030>.
- Weber, P., Zeilhofer, M.F., Martorana, M., Nocera, K., 2022. Regional investigations of polygonal impact craters on the moon and Vesta. *Research Notes AAS* 6 (4), 87. <https://doi.org/10.3847/2515-5172/ac69f3>.
- Weihl, G.T., Leitner, J.J., Firneis, M.G., 2015. Polygonal impact craters on mercury. *Planet. Space Sci.* 111, 77–82.
- Williams, D.A., Buczkowski, D.L., Mest, S.C., Scully, J.E., Platz, T., Kneissl, T., 2018. Introduction: the geologic mapping of Ceres. *Icarus* 316, 1–13. <https://doi.org/10.1016/j.icarus.2017.05.004>.
- Wood, C.A., Head, J.W., Cintala, M.J., 1977. Crater degradation on mercury and the moon—clues to surface evolution. *Lunar Planet. Sci. Conf. Proc.* 8, 3503–3520.
- Yazıcı, I.S., Cheng, H.J., Crane, K.T., Klimczak, C., 2024. Straight impact crater rim segments on mercury. *J. Maps* 20 (1), 2308687. <https://doi.org/10.1080/17445647.2024.2308687>.
- Yingst, R.A., Mest, S.C., Berman, D.C., Garry, W.B., Williams, D.A., Buczkowski, D., Jaumann, R., Pieters, C.M., De Sanctis, M.C., Frigeri, A.L., Le Corre, L., Preusker, F., Raymond, C.A., Reddy, V., Russell, C.T., Roatsch, T., Schenk, P.M., 2014. Geologic mapping of Vesta. *Planet. Space Sci.* 103, 2–23. <https://doi.org/10.1016/j.pss.2013.12.014>.
- Zeilhofer, M.F., Barlow, N.G., 2021a. The characterization and distribution of polygonal impact craters on Ceres and their implications for the Cerean crust. *Icarus* 368, 114586. <https://doi.org/10.1016/j.icarus.2021.114586>.
- Zeilhofer, M.F., Barlow, N.G., 2021b. The morphologic and morphometric characteristics of craters on Ceres and implications for the crust. *Icarus* 368, 114428. <https://doi.org/10.1016/j.icarus.2021.114428>.
- Zellner, B.H., Albrecht, R., Binzel, R.P., Gaffey, M.J., Thomas, P.C., Storrs, A.D., Wells, E. N., 1997. Hubble space telescope images of asteroid 4 Vesta in 1994. *Icarus* 128 (1), 83–87. <https://doi.org/10.1006/icar.1997.5735>.